Mechanisms of Ocean Eddies' Impacts on Lower Trophic Marine Ecosystems in the California Current System

Victoria Boatwright

Advised by: Baylor Fox-Kemper & Peter Olmsted

A Thesis submitted for the degree of
Bachelor of Science

Department of Physics
Georgetown University
Washington, DC
May 2022

Abstract

Physical and biogeochemical processes in the ocean set the Earth's carbon budget and mitigate heat exchanges between the atmosphere and ocean. Past studies have revealed variability in global phytoplankton fields at the mesoscale, correlating with the scale of ocean mesoscale eddies [1]; this impact by mesoscale eddies is thought to derive from tracer transport mechanisms including vertical fluxes, horizontal advection, local stratification, and Ekman pumping. Regional interactions between eddies and phytoplankton are integral to identifying the specific mechanisms underpinning these relationships. In this study, relationships between eddies and chlorophyll are analyzed in the California Current System (CCS) using a high-resolution biophysical regional ocean reanalysis spanning 2013-2021. Spatiotemporal correlations, composite analyses, and timeseries analyses of biogeochemical variables are used to quantify the biophysical interactions occurring within eddies. This study suggests eddy stirring, or the azimuthal component of horizontal advection at occurs at the eddy periphery, drives the majority of chlorophyll spatial distributions in an eddy, but eddies may trap biogeochemical tracers like nutrients and zooplankton in addition to phytoplankton to transport a local ecosystem within an eddy. In composites of over 3,000 eddies, three-dimensional structures show dipole distributions of chloro-

phyll with a maximum in the south (west) side of the cyclonic (anticyclonic) eddy composite core and a minimum in the north (east) side, a pattern which is replicated in the nutrient and zooplankton model fields. Profiles of temperature show a magnifying warm or cold core anomaly with increasing depth in anticyclonic and cyclonic eddies, respectively. Timeseries analysis shows a general trend of constant areal densities of biogeochemical variables throughout an eddy lifetime, in both cyclonic and anticyclonic eddies; however, anomalies within eddies yield overall negative anomaly of nutrients and an overall positive anomaly of zooplankton concentrations within eddies compared to the average regime, with dissimilar trends in anticyclonic versus cyclonic eddies. By identifying eddy stirring and eddy trapping as primary contributors in mesoscale eddy transport of phytoplankton in the CCS, model and observational results in other regions or in different simulations can be compared in order to distinguish eddy-phytoplankton dynamics and to best understand the underpinnings of interactions in long-term, global models.

Contents

Abstract **ii**

Acknowledgements vi

1 Introduction **1**

1.1 Motivation 1

1.2 Objectives 2

2 Background **4**

2.1 Phytoplankton & Marine Ecology 4

2.2 Ocean Eddies 7

2.3 Ocean Modeling & Reanalyses 14

3 Methods **19**

3.1 CCS Physical-Biological Reanalysis 19

3.2 Spatiotemporal Correlations 23

3.3 Eddy Identification and Tracking 24

3.4 Composite Analysis 26

3.5 Time Evolution Analysis 26

4 Results & Analysis **28**

4.1 Spatiotemporal Correlations 28

4.2 Average Eddy Composites 31
4.3 Time Series Analyses 38

5 Discussion **42**

Dedication **44**

References **45**

Acknowledgements

I wish to thank Professor Baylor Fox-Kemper at Brown University for not only his mentorship and feedback, but for welcoming me into his lab group and opening the door into oceanography for me. I further wish to thank Professor Peter Olmsted, who was continuously committed to my progress and invested in my research. I have appreciated his guidance and curiosity - as well as patience - more than I can put into words. Both Prof. Fox-Kemper and Prof. Olmsted have been role models to me and I will continue to look back on the lessons I've learned from them for years and years to come.

I would like to acknowledge Dr. Mike Jacox and Dr. Mike Alexander for advising this work over the previous summer and supporting me in developing my own ideas by encouraging me to pursue this self-motivated project, especially without them having complete expertise on the topic.

I also wish to acknowledge Professor Rhonda Dzakpasu and the rest of the Georgetown University Physics Department for their constant support and tight-knit community. I would also like to thank Paul Hall, the Center for Computation and Visualization at Brown, and the entire Fox-Kemper group that has supported me and given me a research community.

I finally wish to thank my family - especially my mother and grandmother - for their unrelenting confidence and excitement about my work, even when I explained poorly, and my friends who encouraged me and listened to me talk about my research for the past years.

I would like to acknowledge the NOAA Hollings Scholarship Program and the Clare Luce Boothe Program for providing funding for this work.

CHAPTER 1

Introduction

1.1 Motivation

Oceans occupy 70% of the Earth's surface, accounting for the sequestration of 48% of carbon dioxide, and its surface dwellers are responsible for roughly half of atmospheric oxygen [2]. The ocean plays a significant role in climate change through its contribution to absorbing anthropogenic carbon dioxide and heat, maintaining the hydrological cycle, and amplifying positive warming feedback loops [3]. Marine photosynethsizers, or phytoplankton, are an integral component of the global carbon cycle, oxygen production, and marine ecosystems. Considering how phytoplankton account for twice the amount of carbon fixation performed by the open ocean (90% of the ocean surface), it is important to understand the physical factors promoting the growth and abundance of marine primary producers [4]. Phytoplankton are the base of the ocean food chain, meaning that changes in their populations will produce cascading ecosystem effects and potential feedback loops that may accelerate (or mitigate) global warming. Most phytoplankton are drifters, flowing with the currents and depending on ocean flows to provide them with sunlight and nutrients; therefore, it is important to understand the dynamics between physical

ocean phenomena and phytoplankton, especially that of local phenomena that must be parameterized into larger models when the model cannot resolve smaller scale (10-100km) dynamics.

1.2 Objectives

This study looks specifically at the California Current System (CCS), a region with high upwelling and active eddy turbulence, through a data-assimilated model, or a reanalysis, produced by Moore et al at UC Santa Cruz [5]. By focusing on a particular region, regional mechanisms of eddy impacts on phytoplankton and biogeochemical features can be identified. A model reanalysis has never been used for this type of analysis, thereby permitting the study of features like three-dimensional profiles of features that cannot be measured from satellite observations and lack frequent in-situ data sampling, including variables like wind stress, vorticity, zooplankton concentration and nutrient availability. This study has three components:

1. Identification of the 3D profile of phytoplankton distributions within an average CCS eddy through a composite study;

2. Analysis of characteristic eddy factors (lifetime duration, age of observation), external variables (sea surface temperature, nutrients, different species concentrations, phytoplankton predators), and temporal changes (evolution over time) impacting the phytoplankton distributions; and

3. Hypothesis of mechanisms through which the eddies are impacting phytoplankton based on geophysical fluid dynamics of eddies.

Though eddies are ubiquitous in the ocean, their impact on biogeochemical cycling remains unresolved. It is hypothesized that eddies could produce ecological niches to populations lower on the food chain (or, lower trophic populations) by providing nutrient resupply and supporting predator-prey interactions through trapping ambient drifters [6]. As eddies exist at mesoscales (10-100km), their impact needs to be parameterized into global models; in order to parameterize the influence of

eddies, it is imperative to understand the differences in eddy dynamics at different locations (for example, in an active upwelling region like the CCS) and based on different eddy features (i.e., differences between large versus small radius eddies). This study investigates how a regional reanalysis resolves eddy dynamics in its assimilated model-observation fields in order to investigate the underlying physical mechanisms at play and identify resulting effects to biogeochemistry.

CHAPTER 2

Background

2.1 Phytoplankton & Marine Ecology

Phytoplankton are a key group of primary producers (or marine photosynthesizers), which tend to be neutrally buoyant drifters, relying on currents and physical phenomena to keep them in sunlight and provide them with nutrients. Since phytoplankton produce oxygen, sequester carbon, and support higher trophic species (or species higher on the food chain), it is important to understand their response to and dependence on physical ocean phenomena. As coupled ocean models progress, it is necessary to understand the mechanisms of eddy influences on phytoplankton distributions and populations in order to parameterize these interactions in climate models. There are many taxa of phytoplankton, including nanophytoplankton, diatoms, and dinoflagellates, shown in Figure 2.1. Since they are photosynthetic, phytoplankton depend on sunlight; as light decreases exponentially in water, planktons need to stay in upper layers of the ocean near the surface, called the euphotic zone. Their photosynthetic characteristic also means phytoplankton produce chlorophyll, so their concentrations can be aggregately observed through satellite imaging of ocean color, which measures chlorophyll a.

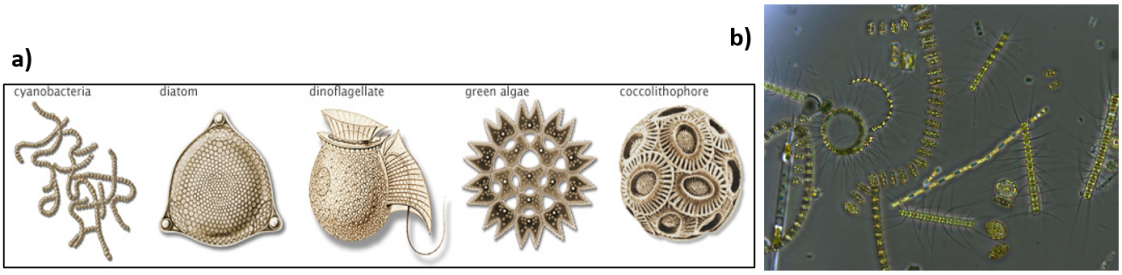

Figure 2.1: Depictions of phytoplankton. a) shows a main categories of phytoplankton types, including cyanobacteria, diatoms, dinoflagellates, green algae, and coccolithophores, adapted from [7]. b) shows a light microscopy image, taken by Stephanie Anderson, of a mixed phytoplankton community [8].

Physical phenomena like eddy-induced stratification and upwelling produced by eddy intensification have been thought to support phytoplankton concentrations by keeping populations near the ocean surface in the sunlight [9]. Phytoplankton also need nutrients—more than just carbon dioxide for photosynthesis—to survive. Though carbon dioxide is generally abundant in ocean waters, common limiting nutrients include inorganic nitrogen, phosphorus, and iron [10]. Generally, nutrients are available in deeper ocean layers beneath the mixed layer where they often will be depleted by biological populations in the euphotic zone (the surface layer where most biological productivity occurs). Nutrients are often more abundant in the zone beneath the euphotic zone, the nutricline, due to geological transfers that happen in deeper waters. The nutricline is the region where most nutrients are stored, at a boundary below which there is a higher concentration of nutrients because these nutrients are limited from transferring to the surface mixed layer by stratification. Current theories propose that nutrients are exported down by the downward transport of sinking particles and detritus (dead organic matter) in addition to the subduction of nutrients by mesoscale frontal structures [11]. Overall, nutrients are restored through the remineralization of sinking detritus and organic matter or by horizontal advection from more nutrient-rich region like continental margins. Therefore, physical mechanisms to resupply surface biological populations with nutrients as well as mechanisms to keep them in the euphotic zone are required for phytoplankton to survive. While studies have shown relationships be-

tween mesoscale eddies—ocean vortices on the scale of 10-100km, described in the next section—and phytoplankton, the similar lifetimes of these phenomena add a component to the story of phytoplankton's likely dependence on eddies. The average timescale of mesoscale eddies can be calculated using their length scale. The length scale (or, approximately the vortex diameter) associated with baroclinic instability in the mixed layer can be related to the horizontal length scale L_s of mesoscale phenomena based on vertical buoyancy gradients, mixed layer depth, and the Coriolis parameter through:

$$L_s = \frac{N * H}{f}, \tag{2.1}$$

where N is the vertical buoyancy gradient; H is the mixed layer depth; and f is the Coriolis parameter which indicates the strength of the Coriolis force (or, the deflection of a moving object due to Earth's rotation). Buoyancy gradients are produced by the density differences between the fluid parcel and the surrounding fluid, producing a force in the direction of the pressure differential. From the length scale L_s and the horizontal propagation speed U of an average mesoscale eddy, the turnover time T_s of an average eddy can be calculated from basic kinematics by:

$$T_s = \frac{L_s}{U}. \tag{2.2}$$

Based on typical values, we can calculate an average length scale of 10-100km and for a propagation speed (or the drift of an eddy center) of roughly 1km per day, the average lifetime of mesoscale eddies lasts roughly 1 month. Phytoplankton blooms typically last around the timescales of 4 weeks, though this lifetime appears to be shortening with increased warming due to air-sea heat fluxes and decreased mixed layer depth [12]. As individual phytoplankton blooms also last on the timescale of weeks or about a month, the similarity of lifetimes between eddies and phytoplankton blooms means that an average mesoscale eddy could support a phytoplankton bloom for roughly its lifetime [13]. Phytoplankton blooms differ in timescales based on their driving mechanisms, which consist of seasonal cycles, higher phytoplankton growth rates than grazing rates, and increased nutrient re-

supply. The driving forces of bottom-up versus top-down control of phytoplankton communities by nutrient availability or zooplankton grazing, respectively, provided by physical forcing is an active area of research. Previous theory, posited by Harald Sverdrup, suggests that phytoplankton blooms initiate after the mixed layer reaches a threshold depth at which growth rates can exceed decay rates based on phytoplankton light, temperature, and nutrient requirements [14]. However, observations have questioned the validity of this theory; instead, a decoupling between zooplankton (or phytoplankton predators, secondary consumers in the marine food web) grazing and phytoplankton growth may be the driver of blooms. This decoupling would stem from either an increase in phytoplankton growth rates or decrease phytoplankton loss rates (presumably by lowered zooplankton grazing), identifying either a bottom-up or a top-down bloom initiation through predator-prey dynamics.

2.2 Ocean Eddies

Coherent ocean eddies at the mesoscale (from 10-100km length scales) are vortices produced by instabilities in horizontal shearing (when a force is applied at a fluids' surface resulting in structural strain) or horizontal density gradients (differences in ocean water's density across the surface due to inhomogeneous heating or salinity). Eddies spin in the clockwise or counterclockwise direction, yielding an anticyclonic or cyclonic eddy, respectively (in the Northern hemisphere). An anticyclonic eddy is associated with a high pressure, positive sea surface height, depressed thermocline/pycnocline which reduces the hydrostatic pressure anomaly at depth, and featuring a pole of downwelling; on the other hand, a cyclonic eddy is associated with low pressure resulting in a surface divergence of water, raising the thermocline and causing a pole of upwelling from deeper waters (Figure 2.2). This convergence or divergence at the surface leaves a signature in sea surface height, allowing satellite observations to identify eddies: high sea surface for anticyclones and low sea surface for cyclones. The thermocline is the ocean boundary between the mixed layer (or, the surface layer) and colder waters beneath where there is the maximum vertical gradient in temperature; above the thermocline, the water column tends

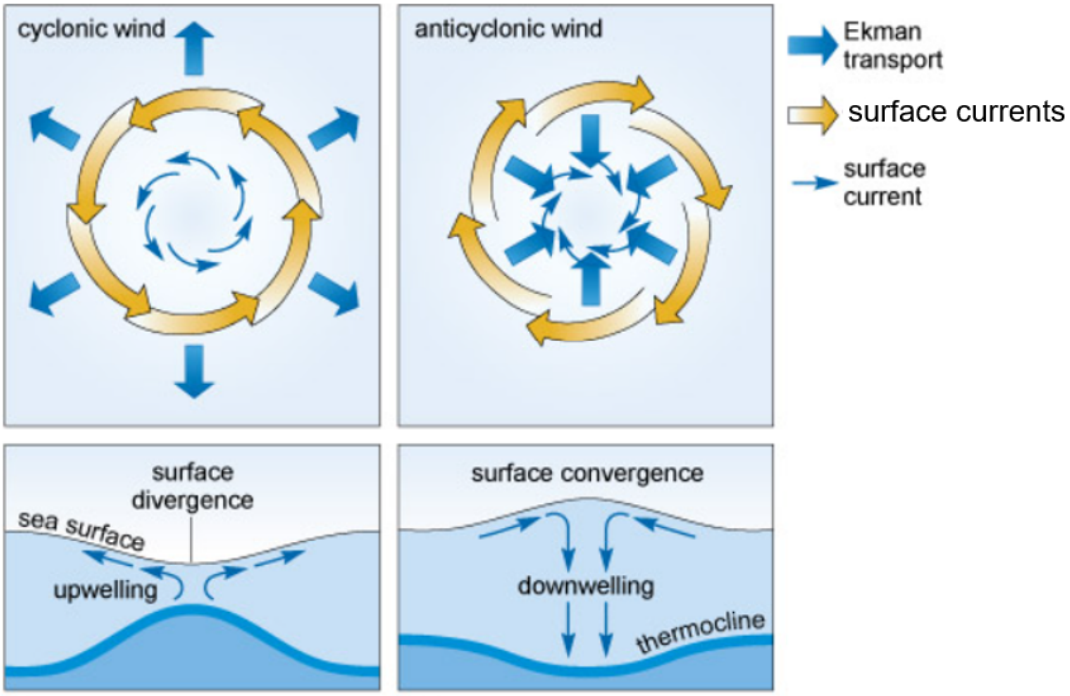

Figure 2.2: Schematic of forces in cyclonic and anticyclonic eddies where a divergent or convergent pressure system yields a vortex spinning in the counterclockwise or clockwise direction due to the Coriolis force. Image taken from [15].

to be well-mixed with a constant temperature, whereas below the thermocline the water's temperature decreases with depth. The thermocline is similar in concept to the pycnocline and the nutricline: the pycnocline is the boundary at which there is the maximum vertical gradient in density, and the nutricline, as discussed in Section 2.1, is the location of the maximum vertical gradient in nutrients.

This study focuses on mesoscale and smaller eddies. Ocean phenomena at this horizontal scale of 10-100km tend to be heavily influenced by the Earth's rotation through the Coriolis effect and buoyancy forces from differentials in density [9]. While the ocean's density only varies by about 3% due to changes in temperature and salinity, these transitions result in important ocean dynamics at large scales like the thermohaline circulation—responsible for global patterns in ocean currents like the Atlantic Meridional Overturning Current—to mesoscale upper ocean dynamics like fronts, eddies, and mixed layer dynamics. The defining characteristics of mesoscale phenomena include the Coriolis parameter, the buoyancy frequency, and the density

stratification. The Coriolis parameter f defined by the cross product of Earth's rotations and the velocity of the object of interest, given by:

$$f = -2(\Omega \times \hat{v}) = 2(\Omega * \frac{sin(latitude)}{\hat{z}}), \tag{2.3}$$

where the object of interest is an isopyncal (or fluid parcel of uniform temperature and density), Ω is Earth's rotation vector, $\hat{v}$ is the unit vector of the velocity of the isopyncal, and $\hat{z}$ is the direction with respect to gravity. The buoyancy frequency N is the ratio of the observed fluid density to the reference fluid density multiplied by the negative acceleration due to gravity, defined by:

$$N = \sqrt{\frac{-g}{\rho}\frac{\partial \rho(z)}{\partial z}}, \tag{2.4}$$

where g is the acceleration due to gravity, ρ is the density of the isopyncal of interest, and $\frac{\partial \rho(z)}{\partial z}$ is the density differential with respect to the vertical [16]. This equation means that the sign of the partial differential equation of density with respect to depth $\frac{\partial \rho(z)}{\partial z}$ can yield two outcomes: a negative differential results in a real angular frequency and thereby an oscillating, controlled density (or buoyancy) whereas a positive differential yields a complex solution and therefore runaway growth—or a completely undamped and unstable fluid. The buoyancy frequency is especially important in the convection of water parcels and stratification of ocean waters. The buoyancy frequency is related to the buoyancy b as the square of the buoyancy frequency is the derivative of buoyancy with respect to depth:

$$N^2 = \frac{db}{dz}, \tag{2.5}$$

as the buoyancy is the ratio of the difference between the density of the fluid parcel of interest and the reference density to the reference density multiplied by the negative acceleration due to gravity, given by:

$$b = -g[\frac{\rho - \rho_0}{\rho_0}]. \tag{2.6}$$

The Coriolis and buoyancy frequency features of fluids define the density strati-

fication parameter δ for mesoscales where the Coriolis parameter over the buoyancy is equivalent to the depth of the phenomena over the horizontal length scale, which at mesoscales will be approximated as much less than one, shown below in:

$$\delta = \frac{f}{b} \approx \frac{D}{L} \ll 1, \tag{2.7}$$

where D is the depth of the phenomenon and L is the horizontal length scale of the phenomenon [9]. In physical terms, the density stratification parameter is the ratio of magnitude of Earth's rotational force on the object to the pressure differentials provided by the density of the fluid compared to its surroundings, resulting in a more stratified phenomenon when the velocity of the phenomenon (contributing to the Coriolis parameter) is greater.

The mesoscale is generally characterized by larger horizontal velocities than vertical ones; for example, a mesoscale eddy with a horizontal radius of 100km will only impact the vertical on the scale of tens of meters. On the other hand, smaller dynamics on the order of 1 m radius will be more three-dimensional and isotropic, having similar magnitudes across any direction of measurement. These dynamics are also influenced by surface wind shear and buoyancy fluxes (or internal instabilities). Fronts, generated from horizontal buoyancy gradients that stay in steady states from the Earth's rotation, are intrinsically linked to eddies since eddies are generated from fronts' baroclinic instabilities—or when perturbations draw energy from the potential energy stored in fronts. Mesoscale eddies introduce shallow instabilities in the mixed layer, re-stratifying the upper ocean and laterally mixing biogeochemical tracers [17]. The mixed layer is the ocean layer where the surface waters are well-mixed, starting at the air-sea boundary and continuing through the region of uniform temperature and salinity (due to intense mixing), which ranges from depths of 10m to over 500m (Figure 2.3) [18]. The mixed layer is important in regulating exchange between the surface and the bottom of the mixed layer, informing to the temperature of the water column, nutrient resupply, and more.

Previously, studies have proposed that mesoscale eddies impact biogeochemical particle tracers by introducing vertical fluxes and deepening the mixed layer into the nutricline, allowing for a resupply of nutrients to euphotic zone (the surface

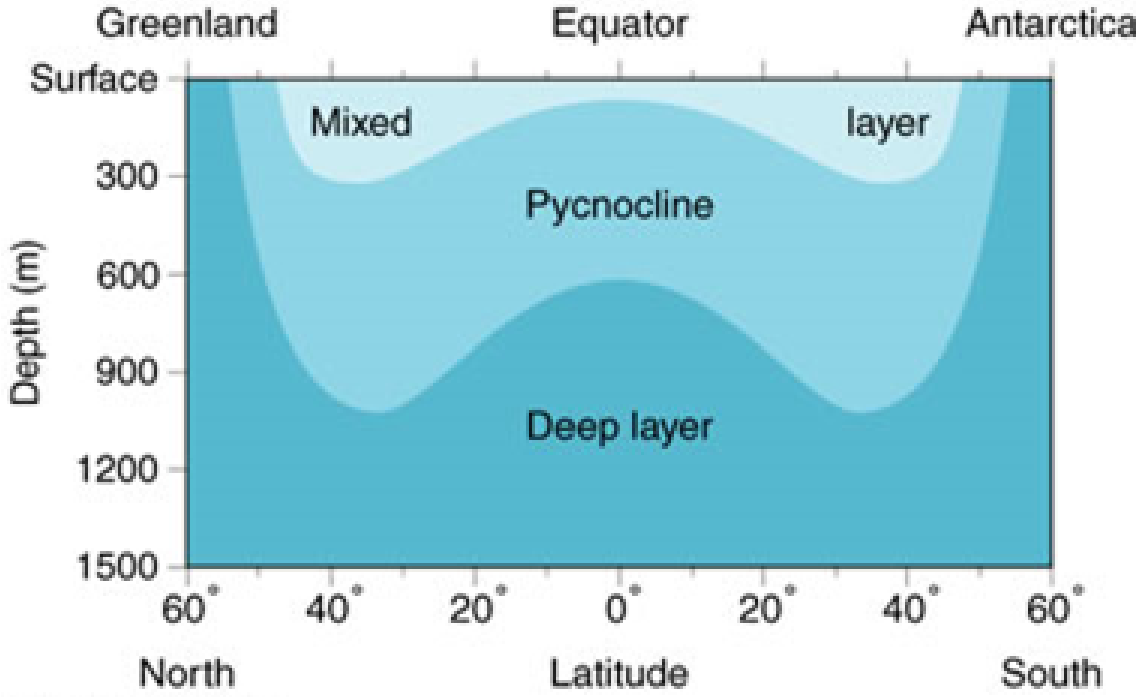

Figure 2.3: Schematic of cross-sectional of an ocean longitudinal profile of different ocean layers from the north pole to the south pole. Though the bottom limit of the depth axis is 1500m, the ocean extends to depths of 4,000m to 6,000m deep. Figure from [22].

layer where most biological concentration exist due to high light exposure) [19] [20]. However, more recent analysis has suggested that the shallow mixed layer would not be able to provide enough resupply from the stratified layer of mesoscale eddies as it will be drawing from a depleted source; this result is proposed from basin-wide studies and mechanistic studies on submesoscale (less than 10km) phenomena [21] [17].

Overall, mesoscale ocean eddies have been shown to impact local biological presence [23] [24] [25] [26] [27]. However, regional differences in eddies' mechanisms and how that impacts biogeochemical variation in phytoplankton signatures or other nutrient profiles are not well understood. Mechanisms proposed to influence ocean tracer transport in eddies include eddy stirring, eddy trapping, eddy intensification, and Ekman pumping [27]. The dominant mechanisms vary according to the region and the local environmental constraints. The horizontal advection of particulate tracers—due to the azimuthal force that comes from the derivative of acceleration

in the non-inertial, rotating frame where S_0 denotes the non-inertial frame of motion:

$$\frac{d^2r}{dt^2}S_0 = \vec{r}'' + \vec{\Omega}' \times r + 2 * (\Omega\vec{r}') + \vec{\Omega} \times (\vec{\Omega} \times \vec{r}), \tag{2.8}$$

where S_0 is the in the inertial, non-rotating frame and the right-hand side is in the non-inertial, rotating frame where $\vec{r}'$ is the velocity of the phenomenon of interest ($\vec{r}''$ is the acceleration) and $\vec{\Omega}$ is the rotation of the system (the azimuthal force is in blue, the Coriolis force is in purple, and the centrifugal force is in green). In models, the time evolution of tracer concentrations follows the advective-diffusion equation:

$$\frac{\partial C}{\partial t} + \vec{v} \cdot \nabla C = -\frac{\partial}{\partial z}(\overline{C'w'} - \nu_\theta \frac{\partial C}{\partial z}) + F_C + D_C, \tag{2.9}$$

where C is the tracer of interest, $\vec{v}$ is the (x, y, z) velocity of the water parcel of interest, w is the vertical velocity, ν_θ is the molecular diffusivity of the tracer, F_C is the effect of forcing, and D_C is the horizontal diffusive term. In eddies, the introduced horizontal advection can be decomposed into two components: eddy stirring and eddy trapping. Eddy stirring occurs at the peripheries of eddies, where the leading edge and trailing edge of an eddy advects existing particulate concentrations into a gradient. There will be a resulting asymmetry due to the trailing edge advecting through an-already passed through particulate field from the leading edge, which—according to quasigeostrophic eddy modeling—yields an overall increase or decrease from the original particulate field [23]. Eddy trapping, on the other hand, occurs when an eddy has a rotational velocity faster than its propagation speed, thereby trapping fluid in its interior through internal horizontal advection in the eddy. Depending on the ambient field of particulates during formation, the eddy interior will propagate an increased or decreased concentration, which will decrease in magnitude over time. The vertical velocities produced by eddies are proportional to the Rossby number, which describes the relative impact that the Coriolis force and inertial forces have on a flow, characterized by:

$$R_0 = \frac{U}{fL}, \tag{2.10}$$

where U is the characteristic velocity and where mesoscale phenomena will fall in the regime of $R_0 \gg 1$. The vertical velocity, W, can be derived using the Rossby number, density stratification, and characteristic velocity by:

$$W \approx R_0 * \delta * U. \tag{2.11}$$

These vertical fluxes result in mechanisms of eddy intensification, a displacement of existing isopyncals, and Ekman pumping (an interaction between wind-driven and eddy-induced surface currents). Eddy intensification generates upwelling and downwelling, respectively, in the formation of an eddy from its signature in the vertical column from surface divergence (in cyclonic eddies) and convergence (in anticyclonic eddies), as explained in Figure 2.2. In contrast, Ekman pumping is produced by the curl of the surface currents due to the interaction between the relative motion of the ocean water from the vorticity of the eddy and the motion from the wind shear of the surface waters, resulting in pumping that induces vertical fluxes within the eddy. The surface stress curl will yield an opposite pole to the vorticity of the eddy in the core, thereby producing Ekman upwelling in anticyclonic eddies and Ekman downwelling in cyclonic eddies. Ekman pumping will often result in gradients in sea surface temperature due to eddy-induced spatial variations from one side of an eddy to another in the face of uniform crosswinds; this gradient of one side of an eddy having double the motion from the combination of wind shear and eddy-induced rotation in the same direction in comparison to a cancelling out on the other side when wind stress and eddy rotation are in the opposite directions.

In terms of phytoplankton concentration, eddy stirring at the periphery is thought to feed resupply of nutrients at the boundaries of eddies, supporting internal phytoplankton concentrations [27]. Eddy intensification would provide vertical fluxes of nutrients or keep phytoplankton concentrations in the euphotic zone. Eddy trapping could support phytoplankton populations by carrying them offshore into more nutrient rich waters. Ekman pumping could maintain phytoplankton concentrations by preserving them in the light and vertically transporting nutrients in anticyclonic eddies. The strength of these impacts varies depending on the regional upwelling system, existing phytoplankton concentrations nearshore, nutrient availability in the

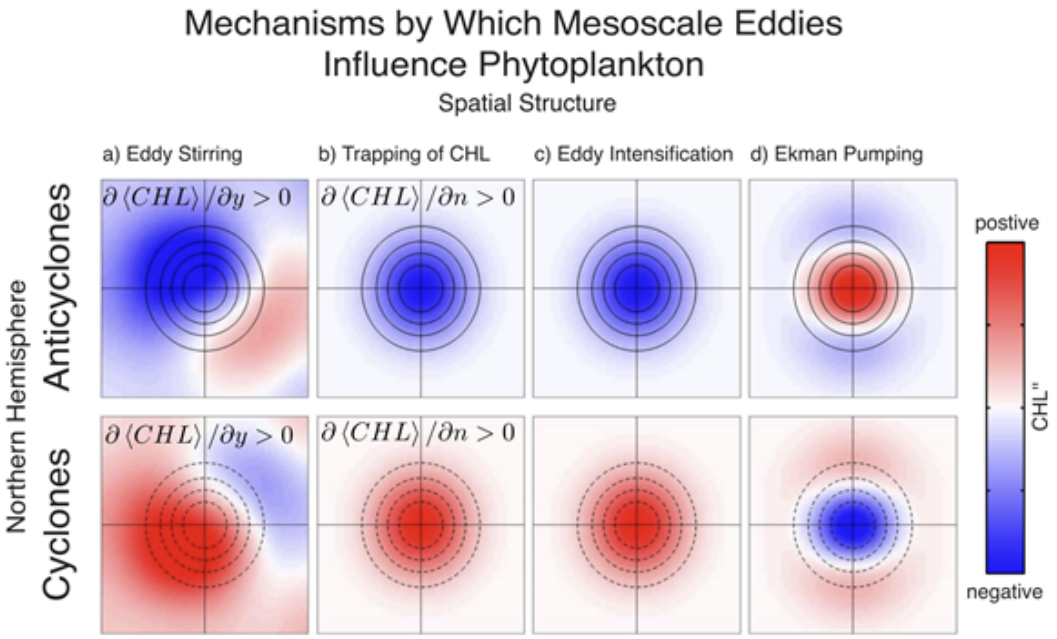

Figure 2.4: Theoretical simulation of the spatial distribution of chlorophyll anomalies within idealized eddies, normalized by eddy length scale. Figure taken from [27].

region, and mixed layer depths. A study by Gaube et al., 2014 proposed theoretical results of chlorophyll concentrations in eddies based on the different mechanisms, shown in Figure 2.4. By identifying the spatial distribution of phytoplankton within eddies, studies can identify which forces play larger roles in different regions or models; Gaube et al.'s study proposed eddy stirring and eddy intensification as dominant factors influencing an average eddy on Earth based on results from satellite measurements of sea surface height and surface chlorophyll. This study will seek to compare the results of an eddy-permitting, data-assimilated model to identify what distribution results from the data-assimilated model equations, thereby revealing which underlying mechanisms are incorporated into the existing model for the California Current System (CCS).

2.3 Ocean Modeling & Reanalyses

Biological and physical coupling in model studies is in its infancy as computing power has only recently reached the resolution capacity to incorporate biological

variables into eddy-resolving models [28]. Currently, we have roughly one tera-grid (or, 10^{12} grid-cells $*$ timesteps) of computational power, yielding global models that can resolve gyres and overturning currents with grid-cells of roughly a degree or less, or regional models that can resolve up to 10km or less (1/10 degree)–depending on the expenses of the model's parameterizations of sub-grid phenomena. Figure 2.5 shows the vast scales in length and lifetime of ocean processes, representing the added difficulty of resolving such variable processes. Global models like the Community Earth System Model (CESM) or MIT's Global Climate Model (MITgcm) to regional models like the Regional Ocean Modeling System (ROMS) vary in their initialization and spin-up as well as their parameterizations depending on the implementation methods, but each model has its own set of ocean circulation, geophysical fluid dynamics equations based on Navier-Stokes momentum principles. Traditional models simulate physical and biological characteristics through partial differential equations of character states at each static grid cell, using parameterizations to estimate sub-grid phenomena. These models are initialized with some state condition (physical and biogeochemical properties) and then run to resolve differential equations of physical and biogeochemical processes; the outputs of models are the calculated evolution of model features (like temperature, salinity, chlorophyll, etc.) at each grid-cell over time. A regional model uses boundary equations and initial conditions to implement model equations at each grid cell. A reanalysis is a data-assimilated model that incorporates observations through numerical assimilation on some interval throughout the model run. Reanalyses are becoming more common for physical models, using satellite measurements of quantities like sea surface height (SSH) and sea surface temperature (SST), in-situ measurements by drifting Argo floats and ship-based measurements, and observation station measurements to incorporate known measurements to bridge the observation-model gap and to confine the model simulation over time to the hindcast scenario. Oceanic models often use atmospheric models to force the surface boundary of the ocean; some models are even coupled between ocean-atmosphere relationships, permitting air-sea interactions.

This study makes use of a ROMS reanalysis model implemented in the California Current System (CCS), from latitude 30°N to 48°N and longitude 115.5° W to

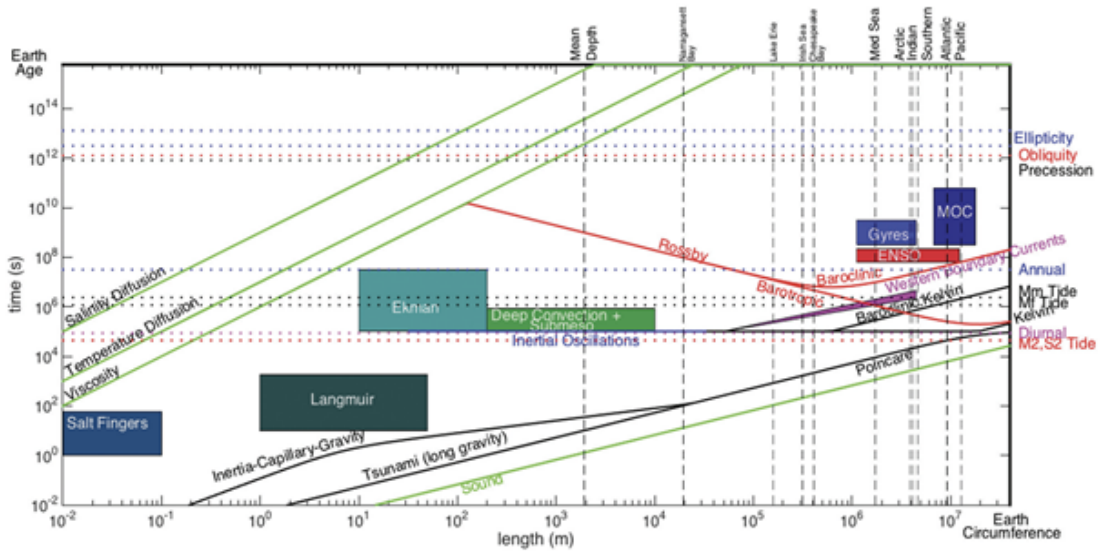

Figure 2.5: Ocean processes and their estimated length scales and timescales, indicating the difficulty of modeling small-scale phenomena in global or even regional models. Figure taken from Haidvogel et al., 2017 [29].

135°W, spanning the North American west coast from Baja California, Mexico, to Washington state, USA, shown in Figure 2.7. This model has grid cells the size of 1/10th degree, or roughly 10km, with 42 terrain-following vertical levels. While the model is run according to the terrain-following grid-cells (demonstrated in Figure 2.6), these model outputs are also interpolated into 11 constant vertical levels, from 250m deep to the surface.

The reanalysis is one of a kind in its assimilation of both physical and *biological* observations using satellite measurements of SST, SSH, sea surface salinity, and *sea surface chlorophyll* (CHL); semi-Lagrangian (or moving with the flow of ocean currents except in the vertical plane) Argo buoys collecting basic physical conditions like temperature, salinity, and pressure; and autonomous ocean glider data. The model is fully coupled between physics and biology: the biology is influenced by physical fields and the physical variables being adjusted by some biological data. Most previous models only assimilate physical observations throughout the model run, so the coupled observational assimilation scheme employed in this model helps to constrain the biogeochemical model fields. The physical components are modeled using general ROMS ocean circulation equations, resolving across 4 dimensions

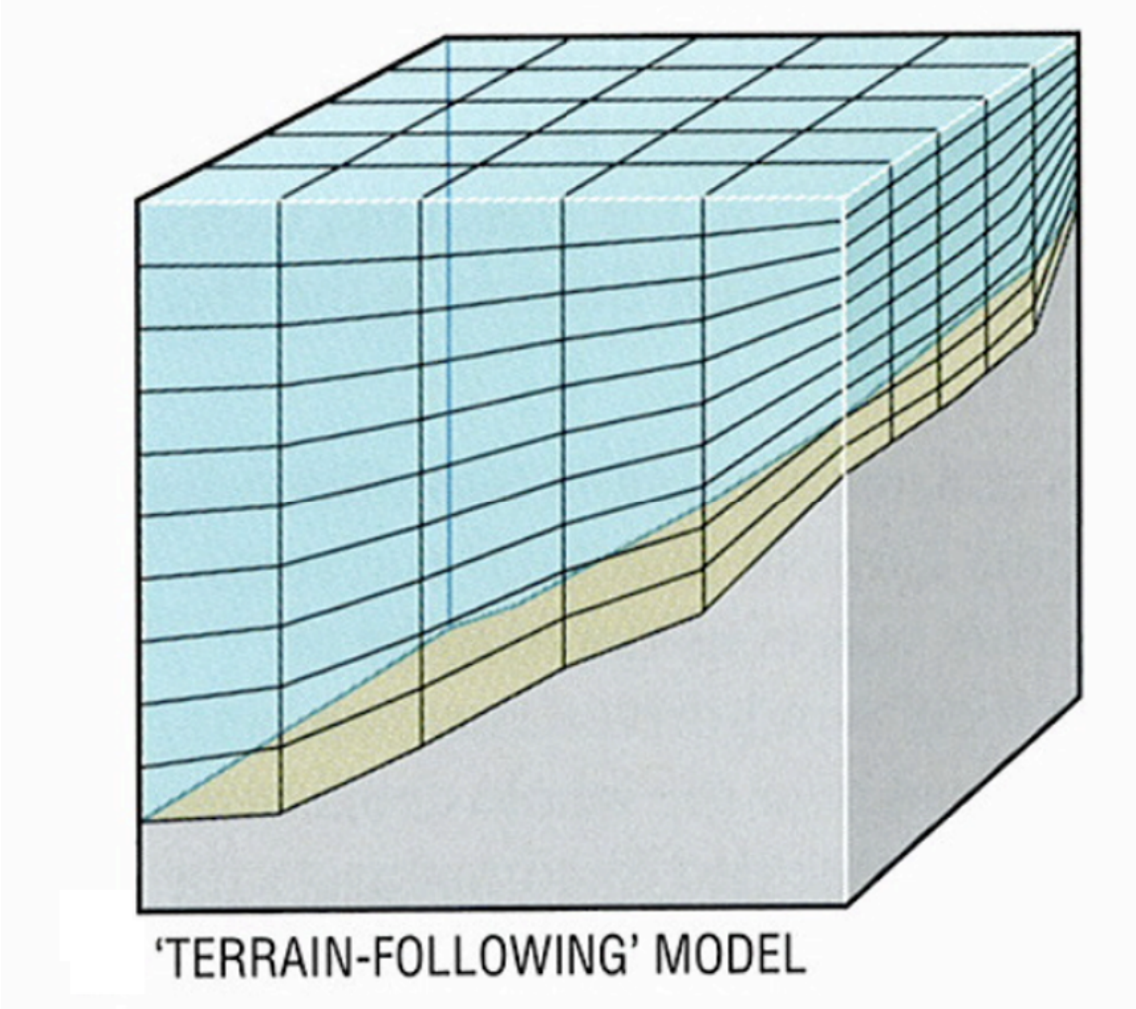

Figure 2.6: Schematic of the grid-cell shape in a terrain-following model. Taken from [30].

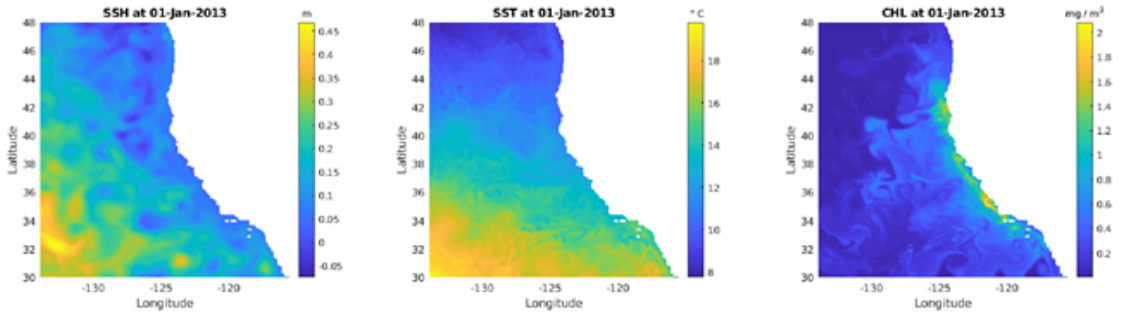

Figure 2.7: Sea surface height, sea surface temperature, and chlorophyll fields produced by the University of California: Santa Cruz's CCS Physical-Biology Reanalysis on January 1, 2013. Area in white is land cover, whereas area in color is ocean regime.

through 42 terrain-following z-levels of depth, x, y, and time. The biological components are modeled by a basic nutrients-phytoplankton-zooplankton (NPZ) model, representing the lower trophic ecosystem. Further information on the model parameters and implementation procedures is detailed in Methods and Neveu et al., 2015 [31].

CHAPTER 3

Methods

3.1 CCS Physical-Biological Reanalysis

The data used for this study comes from a coupled Physical-Biological ROMS Reanalysis of the CCS, spanning the timeframe from 2013 to 2021. The surface ocean is forced by the Coupled Ocean/Atmospheric Mesoscale Prediction System (COAMPS) atmospheric fields produced by a model with assimilated observations, produced by the Naval Research Laboratory. Tides and freshwater inputs from rivers are not included. The outputs of a basin-scale data assimilating model, HYCOM, are used to initialize and set the lateral ocean boundary conditions. The physical state variables resolved in the model include sea surface height, temperature, salinity, meridional (North-South) and zonal (East-West) fluid momentum, and vertical velocity. The fundamental equations of motion for seawater that resolve variables across grid cells in the model include the principal thermodynamic properties. The model calculates changes in density by multiplying the initial density times the divergence of the 3-dimensional velocity, in the form of force equals mass times velocity in:

$$\frac{D\rho}{Dt} = -\rho \nabla \cdot \vec{u} \tag{3.1}$$

(where ρ is the density and $\vec{u}$ is the three-dimensional velocity). The change in temperature is calculated by the compressing force (the partial derivative of temperature with respect to pressure times the derivative of pressure) plus the frictional heat (given by the strain rate times the in-situ density) minus the heat lost to mixing (given by the salt flux times the divergence of the difference in the enthalpy of freshwater and saltwater concentrations) minus the heat flux (given by the divergence of the input heat sources), all normalized by the density times the specific heat, in:

$$\frac{DT}{Dt} = \frac{\partial T}{\partial p}_{\eta,S} * \frac{Dp}{Dt} + \frac{1}{\rho C_p}[-\Delta \cdot (q_{(mol)} + q_{\text{rad}}) + D_{i,j}\sigma_{i,j} - \vec{I_S} \cdot \nabla(h_s - h_w)], \tag{3.2}$$

where T is in-situ temperature, p is pressure, D is the strain rate, I_s is the salt flux, q is input heat, and h is partial enthalpy of saltwater and freshwater, respectively for h_s and h_w. The change in salinity at each grid-cell is calculated by finding the negative divergence of the salt flux divided by the density, as in:

$$\frac{DS}{Dt} = -\frac{1}{\rho}\nabla \cdot \vec{I_S}. \tag{3.3}$$

Then, the Boussinesq system is applied since seawater can be approximated as an incompressible fluid and used to convert potential and kinetic energy through the sinking of dense water and rising of light-weight water. The Boussinesq equations are applied as follows to make density a background, conserved value by:

$$\nabla \cdot \vec{u} \approx 0 \tag{3.4a}$$

$$\frac{D\vec{u}}{Dt} = \frac{1}{\rho_0}\nabla \cdot (-\phi\vec{I} + \sigma_{\text{mol}}) - 2\vec{\Omega} \times \vec{u} + b\hat{k} \tag{3.4b}$$

$$\frac{D\theta}{Dt} \approx \frac{1}{\rho_0 C_p}[-\nabla \cdot (-q_{\text{mol}} + q_{\text{rad}}) + D_{i,j}\sigma_{i,j} - \vec{I_S} \cdot \nabla(h_s - h_w) \tag{3.4c}$$

$$\frac{DS}{Dt} = -\frac{1}{\rho_0}\nabla \cdot \vec{I_S}. \tag{3.4d}$$

In which equations, b is the buoyancy, ϕ is the dynamic pressure ($\phi = \frac{p}{\rho_0}$), ρ_0 is the reference density, Ω is the angular speed of Earth, and $\hat{k}$ is the unit vector defining the vertical direction of the geopotential gradient, or the magnitude of the gravitational force across distances.

In this regional model, there are also boundary equations which force tracer concentrations (particulates which are resolved at each grid-cell of the model, like zooplankton) and flow velocities at the boundaries of the model regime through boundary conditions. These boundary conditions include normal stress, tangential stress, heat, kinematics, and freshwater inputs set by conserved properties at the edges, input evaporation, precipitation, and input wind stress at the air-sea surface boundary, and the lower boundary is set by assuming zero normal (perpendicular) flow at the bottom surface, or a no-normal flow.

In terms of the biological model equations, the ROMS reanalysis employs the North Pacific Ecosystem Model for Understanding Regional Oceanography, "NEMURO." This model resolves 11 state variables, including: nitrate; ammonium; small and large phytoplankton biomass; small, large, and predatory zooplankton biomass; particulate and dissolved organic nitrogen; particulate silica; and silicic acid. The basic NPZ model uses partial differential equations to model the consumption and resupply of nutrients (from upwelling, nutrient remineralization from detritus, and coastal inputs); the growth, predation, and mortality of phytoplankton; and the growth and mortality of zooplankton (grazers and predators of phytoplankton). While the NEMURO equation has more than three state equations to account for different macronutrients and multiple classes of phytoplankton and zooplankton, the basic NPZ equations incorporate three state equations for the nutrient, phytoplankton, and zooplankton concentrations:

$$\frac{d[N]}{dt} = -\frac{V_m[N][P]}{K_s + [N]} + m[P] + g[Z] + (1-\gamma)[Z]R_m(1 - e^{-\Lambda[P]}) \tag{3.5a}$$

$$\frac{d[P]}{dt} = \frac{V_m[N][P]}{K_s + [N]} - m[P] + [Z]R_m(1 - e^{-\Lambda[P]}) \tag{3.5b}$$

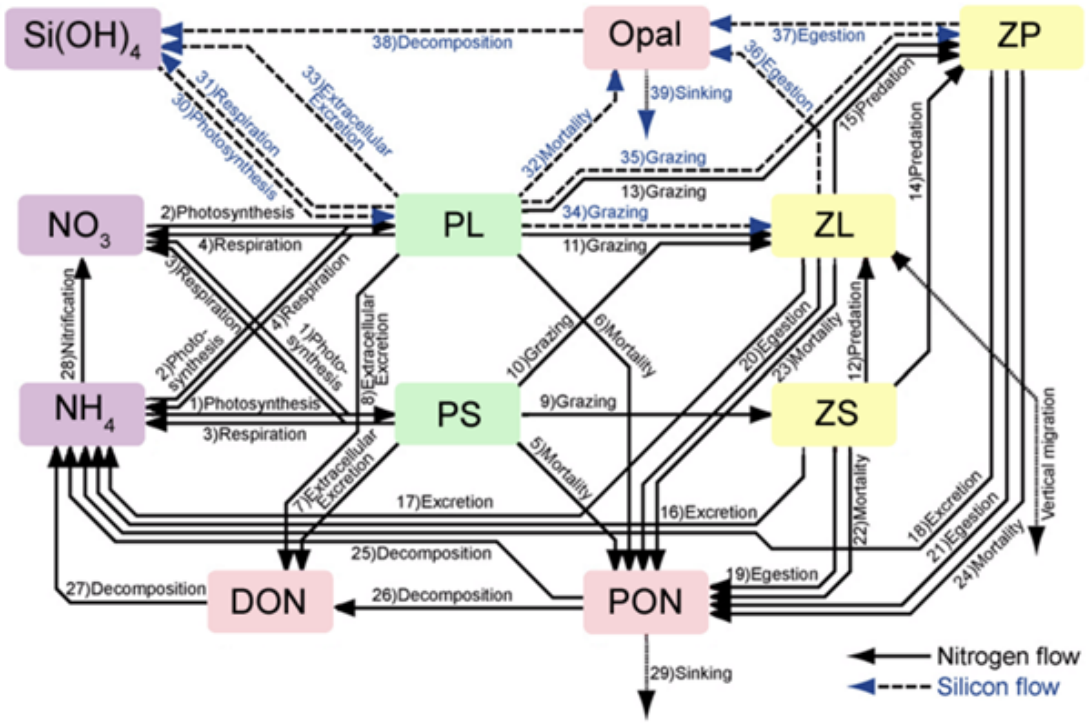

Figure 3.1: Schematic of biogeochemical state variables and the processes that control the rates of exchange between variables in North Pacific Ecosystem Model for Understanding Regional Oceanography (NEMURO). Taken from [32].

$$\frac{d[Z]}{dt} = \Lambda[Z](1 - e^{-\Lambda[P]}) - g[Z]. \tag{3.5c}$$

where the state variables are $[N]$, nutrient concentration; $[P]$, phytoplankton concentration; and $[Z]$, zooplankton concentration; and the rates include: $\frac{V_m[N][P]}{K_s+[N]}$, the nutrient uptake rate; $m[P]$, the rate of phytoplankton mortality; $[Z]R_m(1-e^{-\Lambda[P]})$, the rate of zooplankton grazing; γ, zooplankton growth efficiency; and $g[Z]$, the rate of zooplankton mortality [32]. Figure 3.1 shows a schematic of the exchanges between different biogeochemical state variables and the rates which they are based on. All biological variables are transported by physical ocean currents and turbulence in the model according to the tracer concentration equation 2.8.

The data assimilation performed in this reanalysis is the Incremental, Strong-Constraint 4-D Variational Assimilation (4DVar) method. During assimilation cycles, the 4DVar methods identifies changes to the model ocean state that minimize a cost function (calculated by the sum of squared model-data differences and squared

deviations of a background model ocean state) in order to solve dynamical modeling through adjoined physical equations of the ocean system [31]. The approach is incremental in that it assumes the smallest incremental changes from the background ocean state. The approach is called a strong-constraint method because it ignores errors in physical ocean dynamics, thereby assuming the model equations perfectly represent the physical system and therefore neglect adding an additional forcing term that would fit observational inputs to the model equation [33]. This method leaves only control parameter terms and the initial and boundary conditions in the model equations. On the other hand, the biological assimilation is slightly different since biological ocean variables are not well-represented by Gaussian statistics due to a generally positive skew and zero low bound. Instead of a Gaussian distribution, 4DVar assimilates using a lognormal version of the incremental, strong-constraint method.

3.2 Spatiotemporal Correlations

Correlation coefficients were calculated using the Linear Correlation Coefficient, according to the equation:

$$\rho(a,b) = \frac{[\Sigma(X_{a,i} - X_a)(Y_{b,i} - Y_b)]}{\Sigma(X_{a,i} - \overline{X_a})^2 \Sigma(Y_{b,i} - \overline{Y_b})^2}. \tag{3.6}$$

Spatial correlations were created by calculating correlation coefficients between SSH anomalies and CHL anomalies for each grid cell over all time in the dataset, producing a map of correlations across the regime showing regions of high and low correlations across the dataset. On the other hand, temporal correlations were created by calculating correlation coefficients between SSH anomalies and chlorophyll anomalies for each day in the dataset over the entire regime, creating a timeseries of highly correlated or low correlated time periods. Since eddies move in both space and time, neither type of correlation yielded high correlations because these correlations will not account for an individual eddy lifetime or the spatiotemporal signatures left in chlorophyll or other variables distributions at any one timestep or location; therefore, eddies and their features needed to be isolated in order to follow eddy

tracks and the signature they leave in chlorophyll distributions.

3.3 Eddy Identification and Tracking

Since eddies move in space and time and chlorophyll fields are impacted by other relevant coastal factors, isolating eddy phenomena through eddy detection and tracking was necessary to visualize chlorophyll signatures within eddies. Simple correlations over time or space yielded low correlation coefficients (0.2-0.4) due to the movement of eddies in space and time. Since eddy signatures are visible in SSH from the surface divergence (convergence) of cyclonic (anticyclonic) eddies, SSH anomalies can be used to identify eddies in a field. First, a daily climatology of SSH, SST, and CHL were calculated at each grid cell based on the 8 complete years in the dataset, from 2013-2020. This daily climatology was used to produce anomaly fields of SSH, SST, and chlorophyll by calculating the deviation of the real fields from the daily climatology based on the day of the year, which would remove any seasonal variability from the dataset. A weekly-running mean was applied to the SSH anomaly fields before performing eddy detection to the fields. A sea surface height-based eddy detection algorithm was applied to the dataset, which identifies local maxima (minima) in the SSH anomaly field, then ensures that contours in the SSH anomaly field continue decreasing (increasing) to detect an eddy [34]. Figure 3.2 shows a field of SSH anomalies (SSHa) and the detected anticyclonic and cyclonic eddies on that day to show the validity of the algorithm.

The algorithm processes the SSH anomaly fields in 2 mm contour levels. The parameters of a detected eddy include five requirements: 1) There must be only 1 local extrema within the eddy contour; 2) All pixels in each subsequent level must have decreasing (increasing) SSH anomalies at each contour interval; 3) An eddy is only included if it has more than 10 pixels within its contours and fewer than 10,000 pixels; 4) The cost function for shape deviation from a circle must be less than or equal to 55%, where the cost function is defined as the ratio between the areal sum of deviated from its fitted; and 5) The magnitude of the SSH anomaly must be within 1 to 150cm. The eddy detection algorithm was applied to each timestep

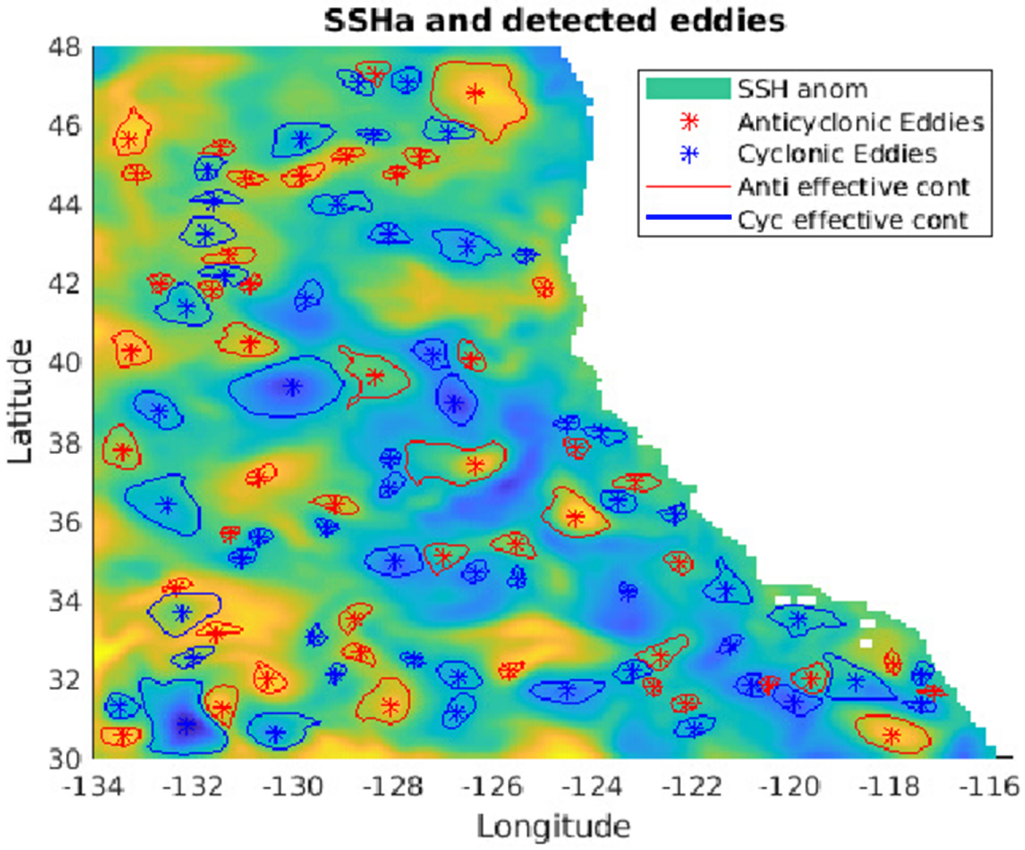

Figure 3.2: Sea surface height anomalies and detected anticyclonic and cyclonic eddies. Cyclonic eddy centers are shown as a blue star with the outermost contour of the eddy marked as a blue line; anticyclonic eddies are shown as a red star with the outermost eddy contour marked as a red line. Fields from May 22, 2021.

(each day) in the dataset, and then compiled to identify tracks in the eddy field. Eddies between time steps that are identified within the same contours are counted to be the same; if more than one eddy falls within the same contour then an eddy will be assigned the same based on dimensionless similarity parameters. If three timesteps pass without an eddy detected in the same contour area, then the eddy track will end; otherwise, the algorithm will fill the contour based on the previous contours. Tracks were dismissed if they lasted fewer than 10 days.

3.4 Composite Analysis

With the dataset of identified eddies, an average eddy profile is calculated over the time period and domain. After normalizing the eddy region based on its effective radius (or the distance from the eddy center to the outermost contour) by interpolating the internal grid-cells onto a high-resolution grid, all eddies are computed into average 81-by-81 pixel fields for variables like SSH anomaly, chlorophyll anomaly, temperature anomaly, and biogeochemical model state variables across eddy observations. Each level in the 11 depths has a composite computed. Other characteristic eddy features—like eddy radius, eddy magnitude, eddy origin location, and eddy lifetime—were used to create different composites and determine whether any feature produces altering impacts on the chlorophyll or state variable signatures.

3.5 Time Evolution Analysis

By indexing eddies based on eddy identification number and observation number within each eddy sequence, biogeochemical concentrations and eddy features are analyzed in their change over time throughout an average eddy life. These timeseries were calculated by summing the internal field of biogeochemical concentrations inside an eddy radius (as examples: chlorophyll, zooplankton species, nutrients) at each day in an eddy's lifetime; the timeseries for evolutions of different variables were computed by aggregating eddies of similar lifetimes and then averaging across those lifetimes. By separating eddies based on their lifetime, there is negligible change

in the size of the dataset (or the number of eddies compiled into the average), thereby avoiding contributions from statistical methods or combining eddy observations from different life phases together. By processing eddies into categories of different lifetimes, differences in long-lasting versus short-lasting eddies can be compared to identify whether eddy longevity impacts biogeochemical processes within an eddy.

CHAPTER 4

Results & Analysis

4.1 Spatiotemporal Correlations

Across the regime of the CCS, the maximum spatial correlation between sea surface height and chlorophyll was just under 0.3 and the minimum was approximately -0.4, shown in Figure 4.1. The more northern region of the CCS shows more positive correlations (suggesting positive SSHa or anticyclones result in increased phytoplankton populations) and a central/southern region of the CCS shows more negative correlations (suggesting negative SSHa or cyclones result in increased phytoplankton populations). However, separating positive and negative anomaly SSHa to isolate anticyclones and cyclones is necessary to draw conclusions from these correlation results; additionally, a maximum magnitude of 0.4 is a relatively low correlation coefficient, signifying there may not be significant relationships between the sea surface height and chlorophyll fields.

Across the duration of the study dataset, the maximum temporal correlation between sea surface height and chlorophyll was just under 0.2 and the minimum was approximately -0.5, shown in Figure 4.2. As the seasonal cycle has been removed by using a calendar climatology to create anomaly fields, there should be no

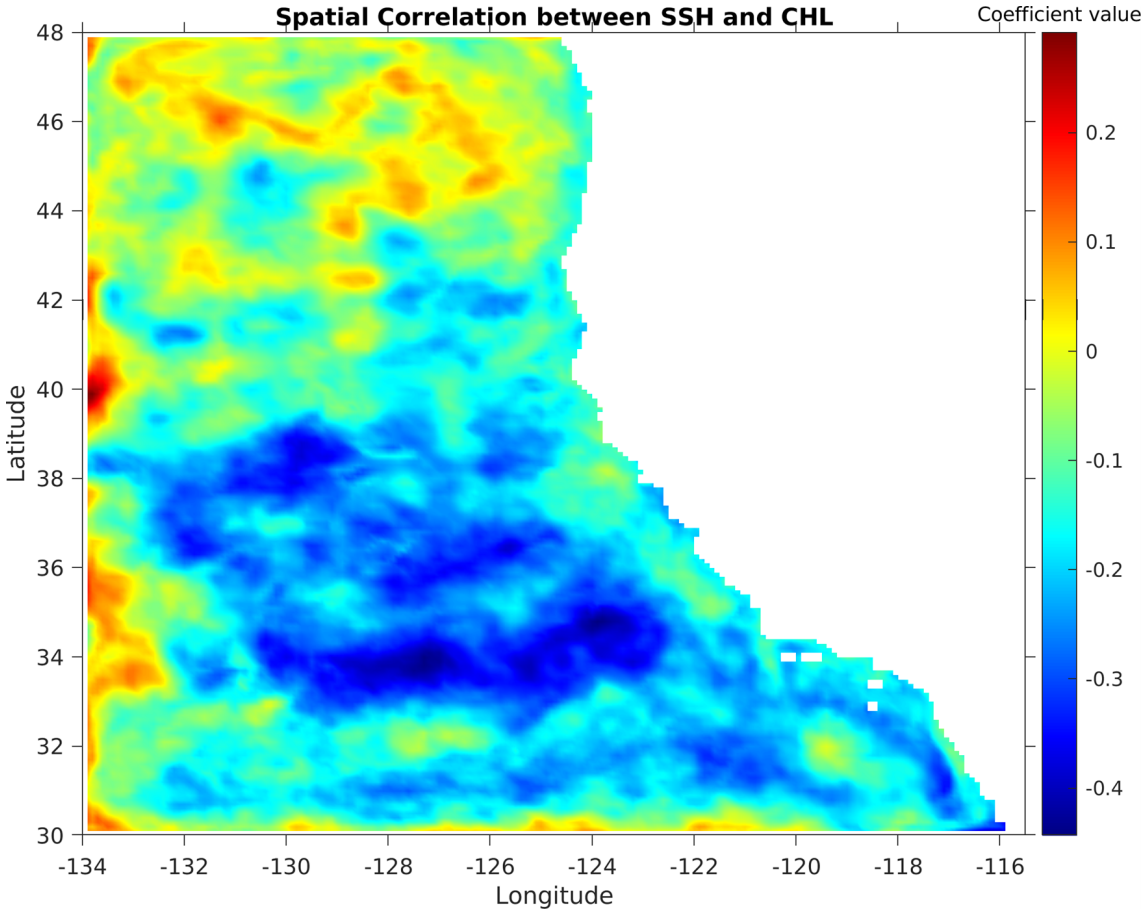

Figure 4.1: Spatial correlations between sea surface height and chlorophyll across the CCS regime. Each grid cell has a correlation coefficient calculated between sea surface height and chlorophyll across the entire time of the dataset, from 2013 to 2021. The maximum coefficient value is 0.2928 and the minimum coefficient value is -0.4432.

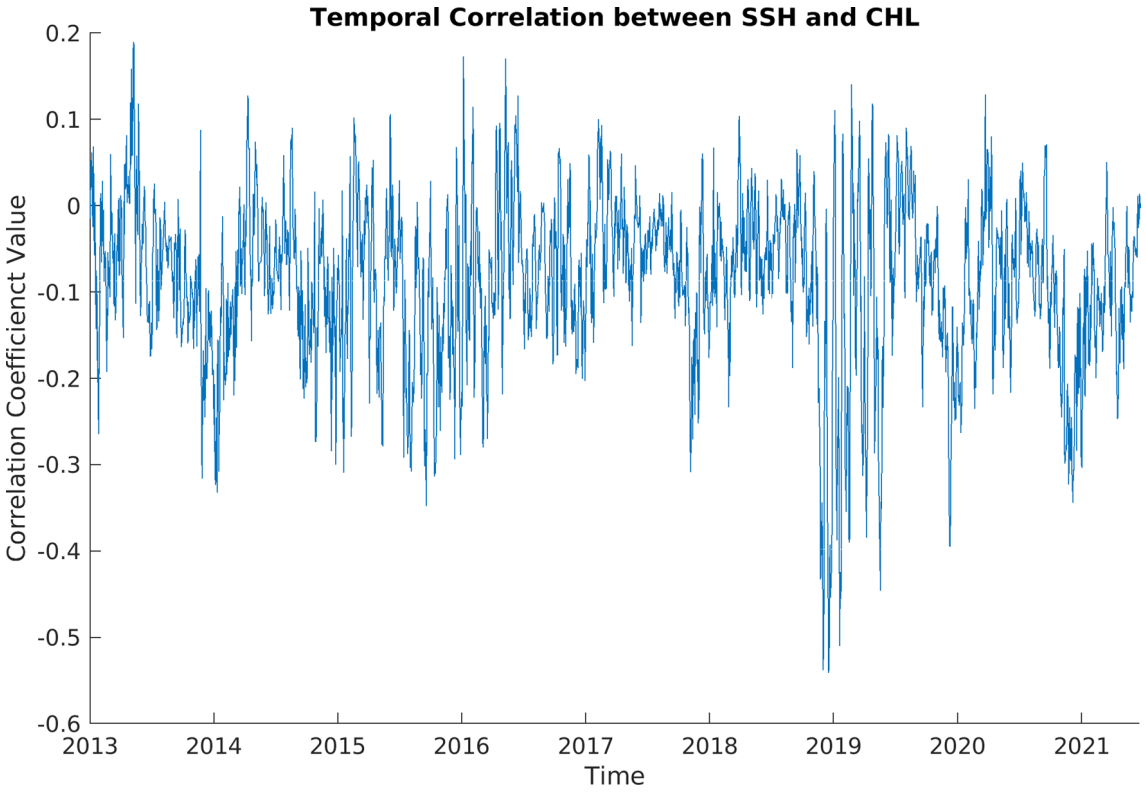

Figure 4.2: Temporal correlations between sea surface height and chlorophyll across the timeline of the dataset, from 2013 to 2021. At each timestep, the correlation coefficient between SSH and CHL is calculated and averaged for all gridcells. The maximum coefficient value is 0.1898 and the minimum coefficient value is -0.5422.

strong seasonality of the correlation between SSH and CHL. The largest negative correlation occurs in 2019 and appears quite extreme, with nearly double the magnitude of the other greatest relationships in time. Again, a maximum magnitude of 0.5 is a relatively low correlation coefficient, signifying there may not be significant relationships between the sea surface height and chlorophyll fields. Considering that eddies move in both space and time, spatiotemporal correlations that cannot analyze within-eddy fields in contrast to non-eddy fields lack the precision to identify and isolate specific eddy-produced dynamics and effects, especially in an active upwelling region where chlorophyll concentrations are impacted by various other mechanisms like coastal processes and runoff. The low coefficients produced by spatiotemporal correlations prompt analyses that can isolate eddy phenomena.

4.2 Average Eddy Composites

The anticyclonic eddy composite (based on 3,533 separate eddies) of SSHa shows a positive anomaly pole of increased SSH, whereas the cyclonic eddy composite (based on 3,718 separate eddies) of SSHa shows a negative anomaly pole of decreased SSH, as expected for anticyclonic and cyclonic eddies, respectively (Figure 4.3a). This result helps to verify the methodology of the composite construction as it aligns with the normal SSHa phenomena of anticyclonic and cyclonic eddies.

The composite of chlorophyll reveals a maximum/minimum dipole in the eddy structure: the anticyclonic composite has a minimum region on the east side of the eddy and a maximum region on the west side of the eddy; on the other hand, the cyclonic composite as a minimum region in the north and a maximum region in the south (Figure 4.3b). It is notable that the signatures in the anticyclonic and cyclonic are not mirror opposites of one another, though the phenomena themselves are opposite in that they are spinning in clockwise and counterclockwise directions as vortices in the water. The maximum positive anomaly is greater in the cyclonic eddy than that of the anticyclonic eddy and the minimum negative anomaly is greater in the anticyclonic eddy than in the cyclonic eddy; this result could indicate that the overall signature of an anticyclonic eddy could leave a negative imprint in spatial concentrations of phytoplankton while a cyclonic eddies could increase the concentrations of phytoplankton along their path in comparison to waters unperturbed by eddies.

The sea surface temperature (SST) composites reveal a somewhat unexpected result of a dipole in their signature rather than a simple core anomaly in the center, shown in Figure 4.3c, where the anticyclonic has a maximum temperature anomaly on the southeast side and the cyclonic has a minimum temperature anomaly on the south side. The more negative anomaly of SST in the cyclonic and the more positive anomaly in the anticyclonic eddy do match the expected phenomena of eddies, where a cyclonic eddy is upwelling cooler, deep waters and therefore would have a cold core and an anticyclonic eddy is downwelling warmer, surface waters producing a warm core.

To further investigate this dipole in the SST composites, depth composites at

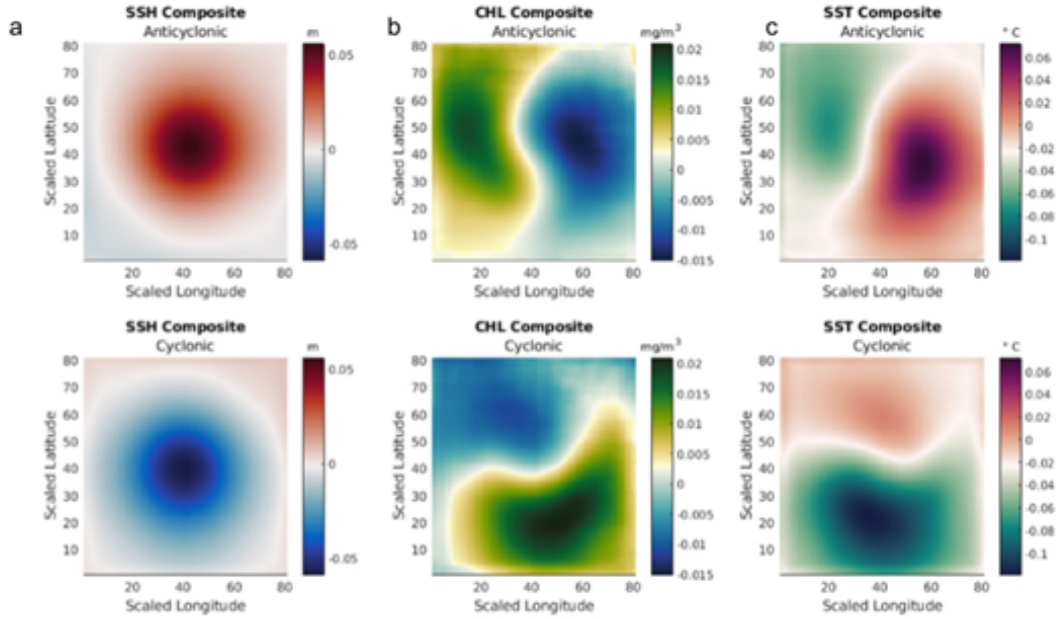

Figure 4.3: Surface composites of anticyclonic and cyclonic eddies. Each variable is the average anomaly field across all eddies' normalized area onto a scaled isotropically onto a longitude and latitude grid. a) shows the sea surface height anomaly composites for anticyclonic and cyclonic eddies on the top and bottom, respectively. b) shows the same format composite result for chlorophyll anomaly, and c) shows the same format composite result for sea surface temperature anomaly.

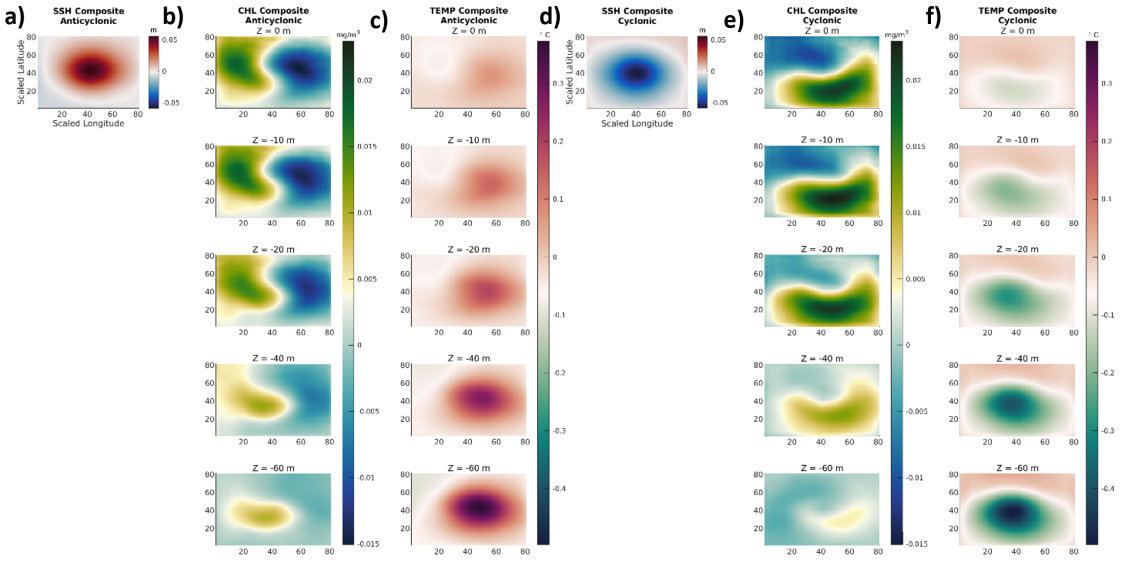

Figure 4.4: Composites at depths of anticyclonic and cyclonic eddies. Each variable is the average anomaly field across all eddies' normalized area at each z-constant level (0, -10m, -20m, -40m, and -60m going from surface to depth from the top to the bottom) and scaled onto longitude and latitude grid. a) and d) show the sea surface height anomaly composites for anticyclonic and cyclonic eddies, respectively. b) and e) show the composite result for chlorophyll anomaly across depths, all set to the same scale across depths and for both anticyclonic and cyclonic eddies. c) and f) show the same format composite result for temperature anomalies across depths.

different Z levels (constant depths beneath the surface) showed the development of a stronger central core in both anticyclonic and cyclonic eddies that match this warm core and cold core (respectively) theory, shown in Figure 4.4c. These depth composites show an increasing magnitude of temperature anomaly with depth, suggesting that the temperature at the surface would have lower anomalies due to surface inputs from radiative forcing and intense mixing at the surface compared to depths where the eddy phenomena dominates the temperature signature. The depth composites of chlorophyll show a decreasing magnitude of anomalies with depth, which can be explained by phytoplankton's dependence on sunlight: there should be exponentially decreasing populations with depth due to light limitation, causing any anomaly in the phytoplankton population to decrease in magnitude, which agrees with the result shown in Figure 4.4b.

At depths, the spatial structures of the chlorophyll signature also change: the anticyclonic eddy composite shows the development of a relatively low positive anomaly

core surrounded by negative anomaly region, while the cyclonic eddy composite develops a more stirred signature where the high versus low anomaly regions further spin around one another with depth. This divergence of spatial structure may suggest a slight difference between anticyclonic and cyclonic eddies in their mechanisms influencing within-eddy phytoplankton concentrations. The magnitude of the chlorophyll anomaly also decreases with depth, which is expected as phytoplankton concentrations generally decrease with depth due to the exponential decrease in light availability with depth, limiting phytoplankton growth and survival. This result shows that eddy tracer transport is not constant across depths; specific mechanisms like stirring might dominate at depths whereas eddy trapping may dominate at the surface.

Composites based on the period of an eddy's life—whether it is early in an eddy's lifetime, around the middle of an eddy's lifetime, or in the end of an eddy's lifetime—indicate changes that occur in the phytoplankton spatial distributions over the course of an eddy life, which could reveal time-calibrated mechanisms. Figure 4.5 shows the development of SSH, phytoplankton, and temperature at different life stages: early in an eddy lifetime (in the first 25th percentile of eddy ages), in the middle of an eddy lifetime (+/- 8 days around the 50th percentile of eddy ages), and late in an eddy lifetime (later than the 75th percentile of eddy ages).

In Figure 4.5, sections a and d show that SSH anomalies increase in magnitude over the life of an eddy. On the other hand, sections b and e show that the magnitude of the phytoplankton concentration anomalies decrease over the lifetime of an eddy, resulting in similar spatial patterns but decrease in strength. This suggests that over time, while continuously advect internal tracers in similar patterns over the course of its life, it may lose some of the internal concentrations that it trapped in the beginning. Finally, sections c and f show that the temperature anomaly in an eddy change over its lifetime, showing a general pattern of increasing anomaly magnitude with time, with the exception of late in life cyclonic temperatures, which show the development of a warm anomaly for most of the eddy. These composites reveal that an eddy is not stagnant throughout its life, maintaining the same pattern, but rather these spatial patterns may increase or decrease in their magnitude as either tracers

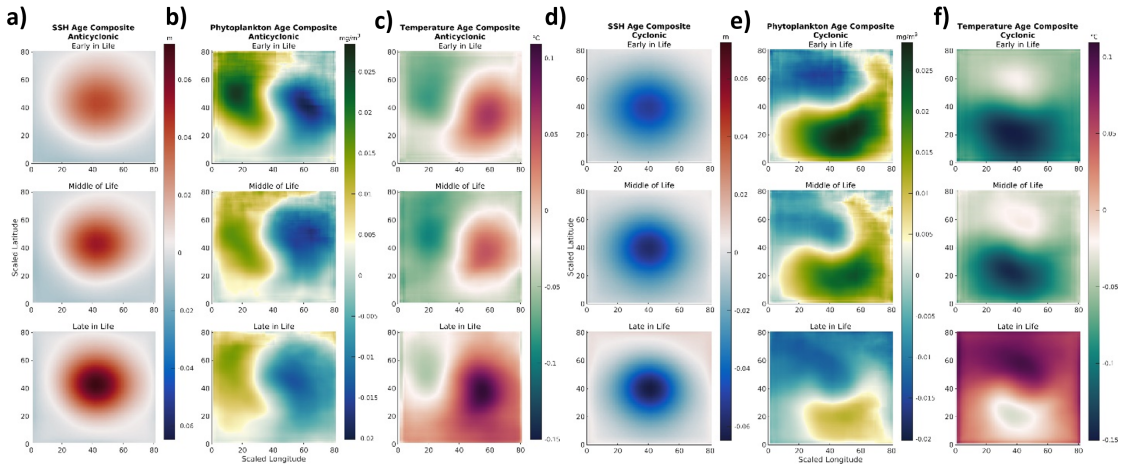

Figure 4.5: Key surface eddy features at different timepoints in an eddy life. The vertical column shows the development of each feature over the eddy lifetime. a-c show anticyclonic eddy composites, and d-f show cyclonic eddy composites. Early in life composites include eddy observations before the 25th percentile of ages, which is 8 for both anticyclonic and cyclonic eddies, including 28,272 observations and 29,752 observations for anticyclonic and cyclonic eddies, respectively. Middle of life composites include eddy observations +/- 4 around the 50th percentile of ages, which is 20 for anticyclonic and 19 for cyclonic eddies, including 14,204 observations and 15,552 observations for anticyclonic and cyclonic eddies, respectively. Late in life composites include eddy observations after the 75th percentile of ages, which is 44 for anticyclonic and 48 for cyclonic eddies, including 31,387 observations and 30,666 observations for anticyclonic and cyclonic eddies, respectively. a and d show the sea surface height average anomaly for each category for anticyclonic and cyclonic eddies, respectively. In the same format, b and e show phytoplankton concentration anomalies (via chlorophyll concentration) while c and f show sea surface temperature anomalies.

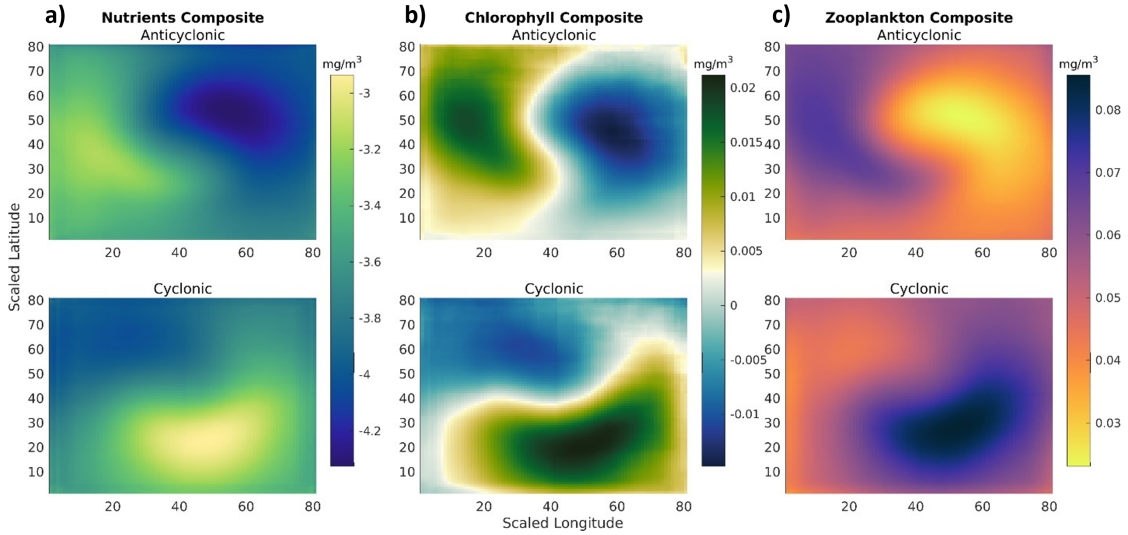

Figure 4.6: Surface composites of biogeochemical variables for anticyclonic and cyclonic eddies. Each variable is the average anomaly field across all eddies' normalized area onto a scaled longitude and latitude grid. a) shows the aggregated nutrient (including nitrate, particulate organic nitrogen, dissolved organic nitrogen, ammonium, silica, and opal) anomaly composites for anticyclonic and cyclonic eddies on the top and bottom, respectively. b) shows the same format composite result for surface chlorophyll anomaly, and c) shows the same format composite result for aggregated fields of zooplankton (microzooplankton, mesozooplankton, and predator zooplankton) anomaly.

diffuse out of or advect out of an eddy or as physical features of an eddy develop and strengthen over its lifetime.

Biogeochemical variables compiled into composites help identify potential nutrient resupply and predator-prey interactions within eddies. Figure 4.6 shows the spatial distribution of nutrients, chlorophyll, and zooplankton at the surface.

Each variable roughly aligns in its structure: high nutrient regions are high in chlorophyll, high chlorophyll regions are high in zooplankton whereas low nutrient regions are low in chlorophyll and low in zooplankton. This alignment suggests a more bottom-up control where phytoplankton generally aggregate where there are nutrients and zooplankton aggregate in the high phytoplankton regions, rather than a top-down control where zooplankton consume away all of the phytoplankton in their region which would result in low phytoplankton concentrations in high zooplankton regions. In terms of the magnitude of each field's anomalies, both anticyclonic and cyclonic eddies result in only negative nutrient anomalies across the

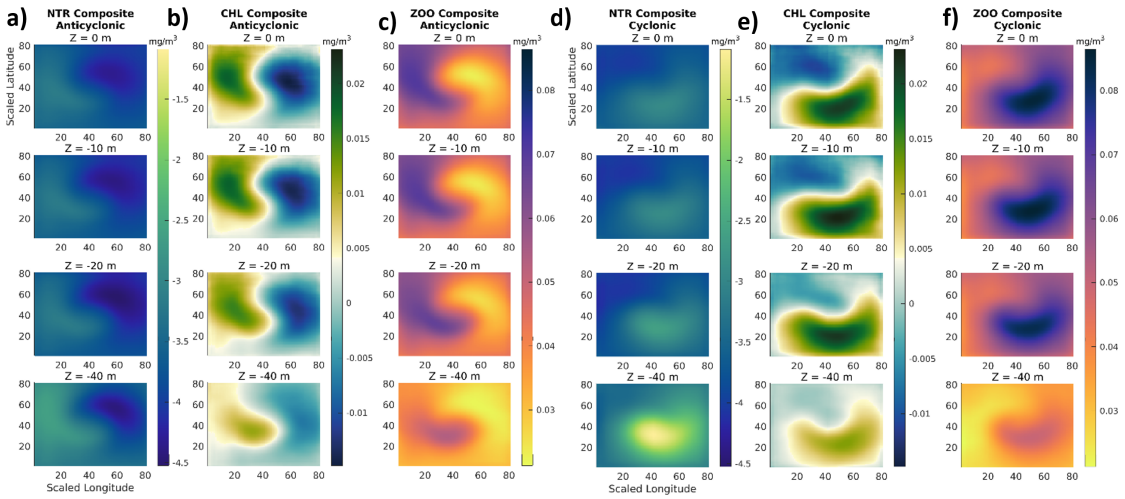

Figure 4.7: Biogeochemical composites at depths for anticyclonic and cyclonic eddies. Each variable is the average anomaly field across all eddies' normalized area at each z-constant level (0, -10m, -20m, and -40m going from surface to depth from the top to the bottom) and scaled onto longitude and latitude grid. a) and d) show the aggregated nutrient anomaly composites for anticyclonic and cyclonic eddies, respectively, sharing the same axes limits across depths and between both anticyclonic and cyclonic composites. b) and e) show the same format result for chlorophyll anomaly across depths. c) and f) show the same format composite result for aggregated zooplankton concentration anomalies across depths.

space within an eddy, whereas chlorophyll has both positive and negative anomalies (discussed previously), and zooplankton has only positive anomalies in both types of eddies. The signs of these anomalies suggest that, at large, nutrient concentrations are decreased in eddies due to the local ecosystem created and their consumption by phytoplankton and zooplankton populations are supported because they can graze on the available phytoplankton. These results suggest that the same eddy transport mechanism is controlling different biogeochemical tracers in this model; the composite anomaly magnitudes also indicates a bottom-up bloom initiation within eddies.

Averaging across depths, a similar general trend in spatial distributions is revealed across nutrient, phytoplankton, and zooplankton fields in terms of horizontal structure (Figure 4.7). Nutrient anomalies increase with depth, likely due to the higher concentration of nutrients at depths from higher geochemical exchanges with sediment and the higher nutrient concentrations in the nutricline. A decrease in the

zooplankton anomalies at depths—similar to that of the phytoplankton anomalies at depths—can be explained by the decreasing concentration of phytoplankton resulting in less food and grazing potential by zooplankton, therefore limiting their populations at depths due to lack of food resources (Figure 4.7c,f). This result suggests that tracer transport across biogeochemical fields retain similar geophysical forcing at depths; differences at depths can be attributed instead to influences from the nutricline (for nutrients) and light availability (for phytoplankton, with cascading effects for zooplankton).

4.3 Time Series Analyses

Changes in concentrations throughout eddy lifetimes reveal relationships between nutrient availability, phytoplankton populations, and zooplankton populations within eddies. The change in area of an eddy is an important physical feature that indicates the relationship between energy supplied to the eddy compared to the energy dissipated from the eddy, which generally dictates its size. Figure 4.8 shows the average change in area across eddies of different lifetimes, including 20-day eddies (272 anticyclonic samples and 308 cyclonic samples), 50-day eddies (111 anticyclonic samples and 125 cyclonic samples), and 100-day eddies (47 anticyclonic samples and 43 cyclonic samples). The averages for each of these categories reveal an overall trend across eddies of an area increase early in life until it reaches a threshold which it maintains for most of its life, and then it declines in size in the end of its life.

The density of nutrients, phytoplankton, and zooplankton stays relatively constant throughout the lifetime of eddies, even across different lifetime categories (Figure 4.9). As cyclonic and anticyclonic eddies are roughly opposite in their spin and vertical transport, the result of similar patterns between anticyclonic and cyclonic eddies across biogeochemical variables is unexpected and may suggest that eddies are trapping ambient fields of biogeochemical tracers in their core during their generation and then pulling these ecosystems along their trajectory through their lifetime.

The net anomaly fields of the biogeochemical tracers, while noisy, show dissimilar patterns in the anticyclonic and cyclonic eddies (Figure 4.10). Due to the noise in

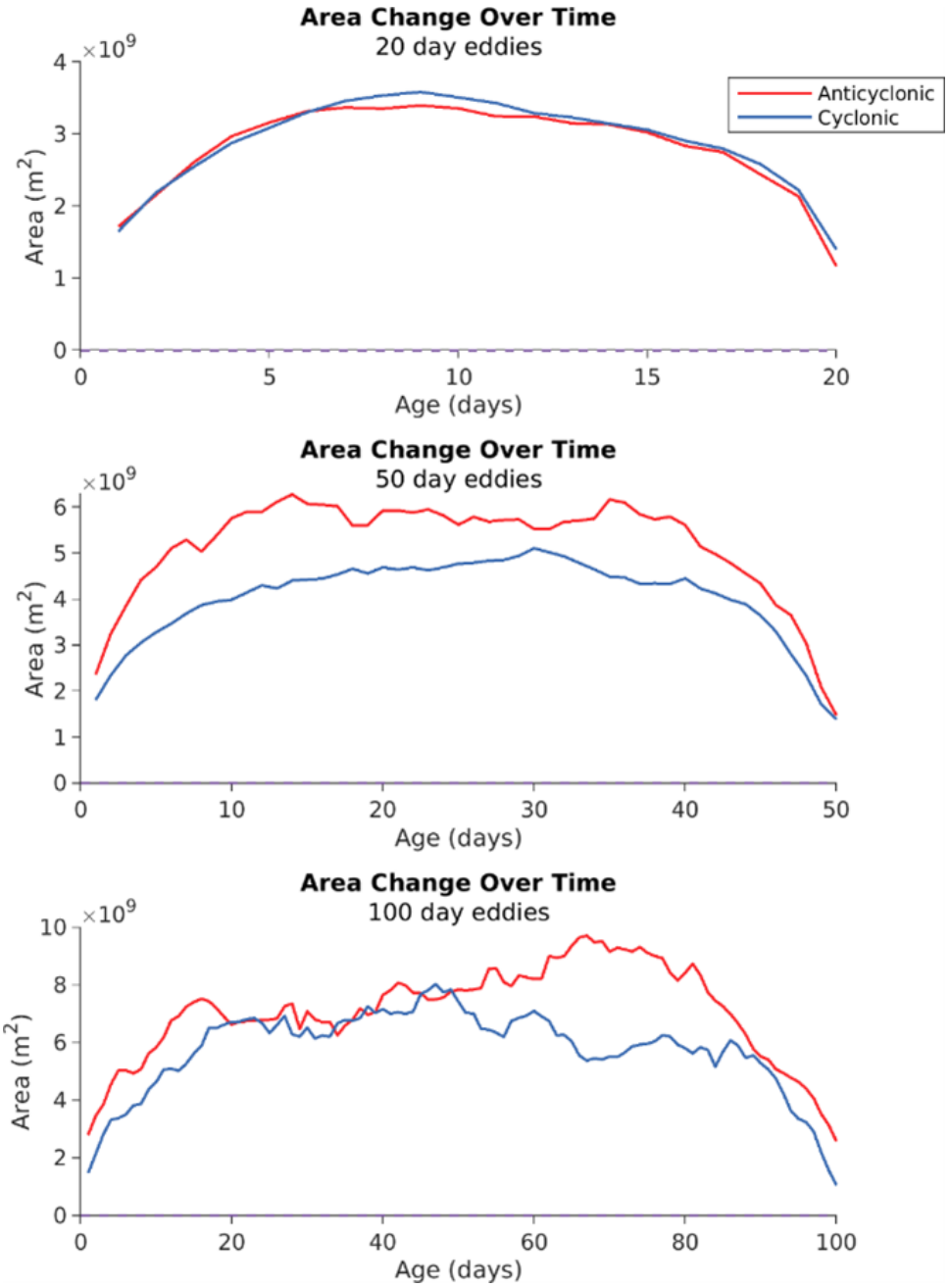

Figure 4.8: Eddy area change over time averaged across 20-day, 50-day, and 100-day eddies. The 20-day category consists of eddies that last 20 +/- 1 day, the 50-day category consists of eddies that last 50 +/- 3 days, and the 100-day category consists of eddies that last 100 +/- 5 days. The 20-day category averages 272 anticyclonic eddies and 308 cyclonic samples, the 50-day category averages 111 anticyclonic samples and 125 cyclonic samples, and the 100-day category averages 47 anticyclonic eddies and 43 cyclonic eddies.

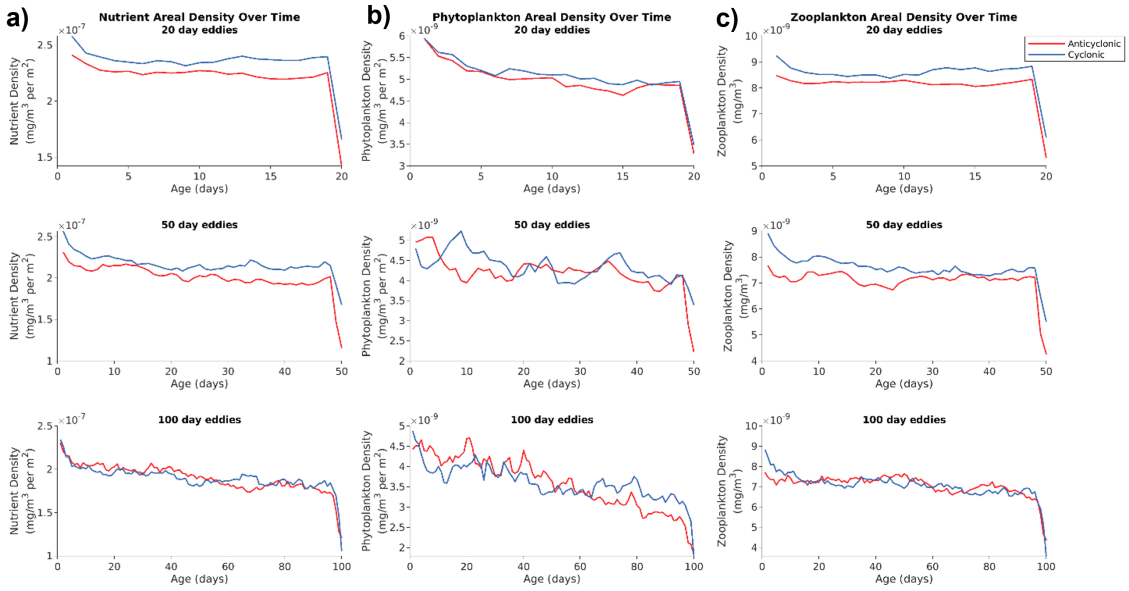

Figure 4.9: Biogeochemical tracer density change over time averaged across 20-day, 50-day, and 100-day eddies. Each tracer field is aggregated within the eddy area and then divided by the area of the eddy at that timestep. a) shows the aggregated nutrient density, b) shows the aggregated chlorophyll density, and c) shows the aggregated zooplankton density. The 20-day category consists of eddies that last 20 +/- 1 day, the 50-day category consists of eddies that last 50 +/- 3 days, and the 100-day category consists of eddies that last 100 +/- 5 days. The 20-day category averages 272 anticyclonic eddies and 308 cyclonic samples, the 50-day category averages 111 anticyclonic samples and 125 cyclonic samples, and the 100-day category averages 47 anticyclonic eddies and 43 cyclonic eddies.

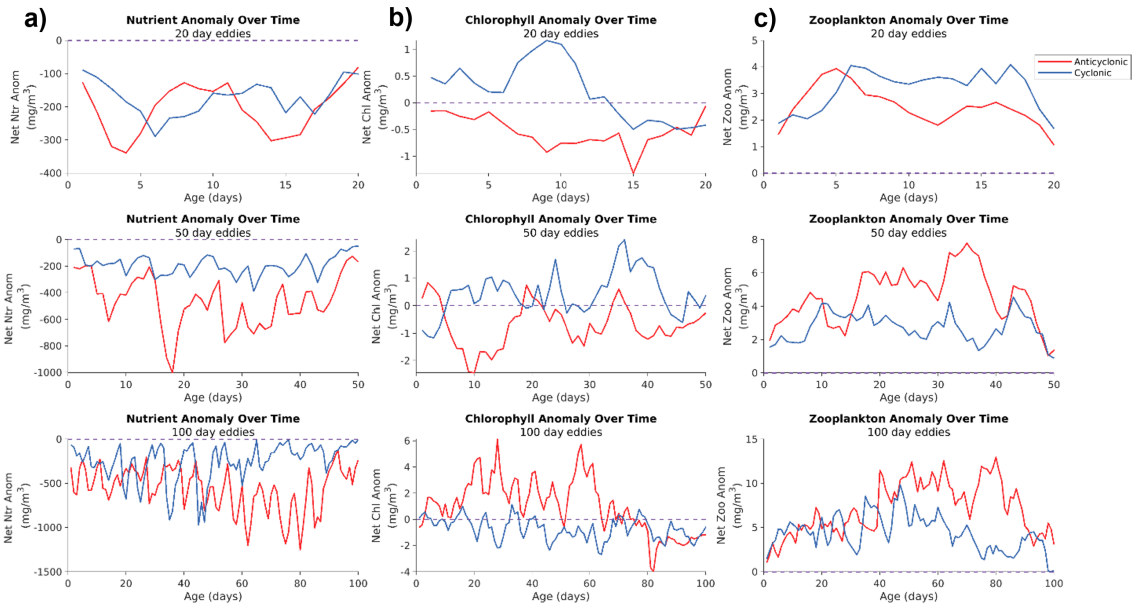

Figure 4.10: Within-eddy biogeochemical tracer anomalies over time averaged across 20-day, 50-day, and 100-day eddies. Each tracer anomaly field is summed to its net value per eddy observation. a) shows the nutrient anomaly evolution, b) shows the phytoplankton anomaly evolution, and c) shows the zooplankton anomaly evolution. The categories are collected by the same method as Figure 4.9 and consist of the same sample size as Figure 4.9.

each timeseries as well as the lack of consistency between eddy lifetime categories, this result presents few unifying conclusions. However, the net anomaly evolution does show that the average within-eddy nutrient anomaly is consistently negative in comparison to the general regime; on the contrast, the average within-eddy zooplankton anomaly is consistently positive throughout all eddy lifetimes. On the other hand, the phytoplankton within-eddy anomaly stays within range of the zero-anomaly line. These results further confirm the incidence of nutrient depletion in eddies and zooplankton population enhancement in eddies.

CHAPTER 5

Discussion

In summary, this work reveals a maximum/minimum dipole of phytoplankton spatial distributions in both anticyclonic and cyclonic eddies, though these spatial patterns are not exactly mirror images of one another (Figure 4.3). An average anticyclonic eddy shows a stronger negative anomaly while an average cyclonic eddy shows a stronger positive anomaly in their phytoplankton fields; though, the magnitude of these phytoplankton anomalies decreases over the lifetime of the eddy (Figure 4.5). Composites of biogeochemical tracers reveal similar spatial patterns of tracer transport within an eddy and that the transport of tracers stays generally consistent across depths (Figures 4.6 & 4.7). Both the magnitude of composite anomalies and the time series of anomalies over eddy lifetimes show that, on average, within-eddy nutrient concentrations are less than anywhere else in the region and within-eddy zooplankton concentrations are higher than anywhere else in the region (Figure 4.10). Throughout the life of an eddy, biogeochemical tracers remain relatively constant in terms of their areal density within an eddy (Figure 4.9).

These results are informative by providing insights into the interactions between eddies and biogeochemical tracers in an eddy-resolving model reanalysis. First, the distribution of phytoplankton within the anticyclonic and cyclonic eddies suggest

eddy stirring as a likely candidate for tracer transport within eddies, while the constant field of biogeochemical densities in both anticyclonic and cyclonic eddies over eddy lifetimes suggests eddy trapping may be the underlying mechanism maintaining persistent communities within eddies from their initial ambient field. Identifying these eddy tracer transport mechanisms is useful in parameterizing this phenomenon in models at lower resolutions, like global models that are not eddy-resolving. Currently, models with a coarser resolution use large-scale gradients of mean tracer concentrations to parameterize turbulent transport [35]. Reactive tracers, like nutrients and phytoplankton, appear to depend on their initial ambient field that is transported along with eddies, which indicate that tracers would move along eddy trajectories. However, further study on the ambient fields of nutrients, phytoplankton, and zooplankton at the initial generation of an eddy should be performed to validate the process of an eddy transporting all the reactive tracers (nutrients, phytoplankton, and zooplankton) from its initial ambient field or whether one tracer is more important.

Additionally, the result of an average negative within-eddy nutrient anomaly compared to the CCS region and the result of an average positive within-eddy zooplankton anomaly compared to the CCS region suggest that eddies are providing a region for interaction between trophic levels, potentially permitting a phytoplankton-induced drawdown of nutrients and a growth opportunity for zooplankton communities through grazing within eddies. This result could indicate that within eddy zooplankton blooms are occurring on timescales based on eddy lifetimes. As short-term and sporadic phytoplankton blooms achieve unexplained growth rates, these localized spikes in biomass could be related to the advective processes provided by eddies [13]. The relationships between nutrient availability and predator grazing in an eddy could provide insights into the influence of bottom-up versus top-down control for short-term and mesoscale biomass blooms.

Dedication

This work is dedicated to my dad, Bill Boatwright.

A Sailor Return To Sea
A sailor return to an ocean
And always live in our memories
It was a true pleasure
To have known you
You are now sleeping peacefully
You are singing in heaven
.
Adapted from Ahmed Shiddiq

Bibliography

[1] Martin, A. P. (2003). “Phytoplankton Patchiness: The Role of Lateral Stirring and Mixing.” *Progress in Oceanography*, vol. 57, no. 2, pp. 125–74. https://doi.org/10.1016/S0079-6611(03)00085-5. (document)

[2] Falkowski, P. (2012). ”Ocean science: the power of plankton.” *Nature*, 483(7387), S17-S20. https://doi.org/10.1038/483S17a. 1.1

[3] IPCC. (2019). ”IPCC Special Report on the Ocean and Cryosphere in a Changing Climate” [H.-O. Pörtner, D.C. Roberts, V. Masson-Delmotte, P. Zhai, M. Tignor, E. Poloczanska, K. Mintenbeck, A. Alegría, M. Nicolai, A. Okem, J. Petzold, B. Rama, N.M. Weyer (eds.)]. 1.1

[4] Martin, J. H., Knauer, G. A., Karl, D. M., & Broenkow, W. W. (1987). ”VERTEX: carbon cycling in the northeast Pacific.Deep Sea Research Part A.” *Oceanographic Research Papers*, 34(2), 267-285. https://www.whoi.edu/cms/files/MartinKnauerKarlCarbonVertexDSR198752929.pdf. 1.1

[5] Oke, P. R., Larnicol, G., Jones, E. M., Kourafalou, V., Sperrevik, A. K., Carse, F., et al. (2015). ”Assessing the impact of observations on ocean forecasts and reanalyses: Part 2, Regional Applications.” *Journal of Operational Oceanography*, 8(sup1), s63-s79. https://doi.org/10.1080/1755876X.2015.1022080. 1.2

[6] Bracco, A., Provenzale, A., & Scheuring, I. (2000). ”Mesoscale vortices and the paradox of the plankton.” *Proc Biol Sci*, 267(1454):1795-800. https://doi.org/10.1098/rspb.2000.1212. 1.2

[7] Lindsey, Rebecca, & Michon Scott. (2010). ”What Are Phytoplankton?” NASA Earth Observatory. https://earthobservatory.nasa.gov/features/Phytoplankton. 2.1

[8] Siegel, Dave. (2018). “Just Sit Right Back and You’ll Hear a Tale, a Tale of a Plankton Trip.” NASA Earth Expeditions, NASA.

https://blogs.nasa.gov/earthexpeditions/2018/08/15/just-sit-right-back-and-youll-hear-a-tale-a-tale-of-a-plankton-trip/. 2.1

[9] Mahadevan, A. (2016). "The impact of submesoscale physics on primary productivity of plankton." *Annual review of marine science*, 8, 161-184. https://doi.org/10.1146/annurev-marine-010814-015912. 2.1, 2.2, 2.2

[10] Bristow, L. A., Mohr, W., Ahmerkamp, S., & Kuypers, MMM. (2017). "Nutrients that limit growth in the ocean." *Curr Biol*, 27(11):R474-R478. https://doi.org/10.1016/j.cub.2017.03.030. 2.1

[11] Stukel, M. R., Aluwihare, L. I., Barbeau, K. A., Chekalyuk, A. M., Goericke, R., Miller, A. J., ... & Landry, M. R. (2017). "Mesoscale ocean fronts enhance carbon export due to gravitational sinking and subduction." *Proceedings of the National Academy of Sciences*, 114(6), 1252-1257. https://doi.org/10.1073/pnas.1609435114. 2.1

[12] Gittings, J. A., Raitsos, D. E., Krokos, G., & Hoteit, I. (2018). "Impacts of warming on phytoplankton abundance and phenology in a typical tropical marine ecosystem." *Scientific reports*, 8(1), 1-12. https://doi.org/10.1038/s41598-018-20560-5 2.1

[13] Isles, Peter DF, & Pomati, F. (2021). "An Operational Framework for Defining and Forecasting Phytoplankton Blooms." *Frontiers in Ecology and the Environment*, vol. 19, no. 8: pp. 443–50. https://doi.org/10.1002/fee.2376. 2.1, 5

[14] Behrenfeld, Michael J. (2010). "Abandoning Sverdrup's Critical Depth Hypothesis on Phytoplankton Blooms." *Ecology*, vol. 91, no. 4: pp. 977–89. https://doi.org/10.1890/09-1207.1. 2.1

[15] The Open University. '4.4 Divergence and convergence,' https://www.open.edu/openlearn/science-maths-technology/the-oceans/content-section-4.4 2.2

[16] Thomas, L. N., Tandon, A., & Mahadevan, A. (2008). "Submesoscale processes and dynamics." *Ocean modeling in an Eddying Regime*, 177, 17-38. https://doi.org/10.1029/177GM04. 2.2

[17] Fox-Kemper, B., Ferrari, R., & Hallberg, R. (2008). "Parameterization of mixed layer eddies. Part I: Theory and diagnosis." *Journal of Physical Oceanography*, 38(6), 1145-1165. https://doi.org/10.1175/2007JPO3792.1. 2.2

[18] de Boyer Montégut, C., Madec, G., Fischer, A. S., Lazar, A., & Iudicone, D. (2004). "Mixed layer depth over the global ocean: An examination of profile data and a profile-based climatology." *Journal of Geophysical Research: Oceans*, 109(C12). https://doi.org/10.1029/2004JC002378. 2.2

[19] McGillicuddy Jr, D. J., & Robinson, A. R. (1997). "Eddy-induced nutrient supply and new production in the Sargasso Sea. *Deep Sea Research Part I: Oceanographic Research Papers*, 44(8), 1427-1450. https://doi.org/10.1016/S0967-0637(97)00024-1. 2.2

[20] McGillicuddy, D. J., Robinson, A. R., Siegel, D. A., Jannasch, H. W., Johnson, R., Dickey, T. D., ... & Knap, A. H. (1998). "Influence of mesoscale eddies on new production in the Sargasso Sea." *Nature*, 394(6690), 263-266. https://doi.org/10.1038/28367. 2.2

[21] Mahadevan, A., & Tandon, A. (2006). "An analysis of mechanisms for submesoscale vertical motion at ocean fronts." *Ocean Modelling*, 14(3-4), 241-256. https://doi.org/10.1016/j.ocemod.2006.05.006 2.2

[22] NASA. "Ocean's Vertical Structure." Ocean Motion, http://oceanmotion.org/html/background/ocean-vertical-structure.htm. Accessed 27 Apr. 2022. 2.3

[23] Chelton, D. B., Gaube, P., Schlax, M. G., Early, J. J., & Samelson, R. M. (2011). "The influence of nonlinear mesoscale eddies on near-surface oceanic chlorophyll." *Science*, 334(6054), 328-332. https://doi.org/10.1126/science.1208897. 2.2, 2.2

[24] Frenger, I., Münnich, M., & Gruber, N. (2018). "Imprint of Southern Ocean mesoscale eddies on chlorophyll." *Biogeosciences*, 15(15), 4781-4798. https://doi.org/10.5194/bg-15-4781-2018. 2.2

[25] Mahadevan, A., D'asaro, E., Lee, C., & Perry, M. J. (2012). "Eddy-driven stratification initiates North Atlantic spring phytoplankton blooms." *Science*, 337(6090), 54-58. https://doi.org/10.1126/science.1218740. 2.2

[26] Garçon, V. C., Oschlies, A., Doney, S. C., McGillicuddy, D., & Waniek, J. (2001). "The role of mesoscale variability on plankton dynamics in the North Atlantic." *Deep Sea Research Part II: Topical Studies in Oceanography*, 48(10), 2199-2226. https://doi.org/10.1016/S0967-0645(00)00183-1. 2.2

[27] Gaube, P., McGillicuddy Jr, D. J., Chelton, D. B., Behrenfeld, M. J., & Strutton, P. G. (2014). "Regional variations in the influence of mesoscale eddies on near-surface chlorophyll." *Journal of Geophysical Research: Oceans*, 119(12), 8195-8220. https://doi.org/10.1002/2014JC010111. 2.2, 2.2, 2.4

[28] Fox-Kemper, B. (2018). "Notions for the motions of the oceans." *New Frontiers in Operational Oceanography*, 27-74. https://doi.org/10.17125/gov2018.ch02. 2.3

[29] Haidvogel, D. B., Curchitser, E. N., Danilov, S., & Fox-Kemper, B. (2017). "Numerical modelling in a multiscale ocean." *Journal of Marine Research*, 75(6), 683-725. https://doi.org/10.1357/002224017823523964. 2.5

[30] Brown, Evelyn, et al. "Ocean Circulation." 1989. 2nd ed., Butterworth-Heinemann, 2001. 2.6

[31] Neveu, E., Moore, A. M., Edwards, C. A., Fiechter, J., Drake, P., Crawford, W. J., ... & Nuss, E. (2016). "An historical analysis of the California Current circulation using ROMS 4D-Var: System configuration and diagnostics." *Ocean Modelling*, 99, 133-151. https://doi.org/10.1016/j.ocemod.2015.11.012. 2.3, 3.1

[32] Hedstrom, K. (2011). An Overview of Biogeochemical Modeling in ROMS. Arctic Region Supercomputing Center. https://www.myroms.org/wiki/images/0/04/Ecosystem.pdf 3.1, 3.1

[33] Di Lorenzo, Emanuele, et al. (2007). "Weak and Strong Constraint Data Assimilation in the Inverse Regional Ocean Modeling System (ROMS): Development and Application for a Baroclinic Coastal Upwelling System." *Ocean Modelling*, vol. 16, no. 3–4: pp. 160–87. https://doi.org/10.1016/j.ocemod.2006.08.002. 3.1

[34] Mason, E., Pascual, A., McWilliams, J. C. (2014). "A new sea surface height–based code for oceanic mesoscale eddy tracking." *Journal of Atmospheric and Oceanic Technology*, 31(5), 1181-1188. https://doi.org/10.1175/JTECH-D-14-00019.1. 3.3

[35] Prend, Channing J., et al. (2021). "Parameterizing Eddy Transport of Biogeochemical Tracers." *Geophysical Research Letters*, vol. 48, no. 21. https://doi.org/10.1029/2021GL094405. 5